LIBS analysis of tritium in thin film-type samples

Aurélien Favre, Arnaud Bultel, Mickael Payet, Stéphane Vartanian, Sébastien Garcia-Argote, Vincent Morel, Elodie Bernard, Sabina Markelj, Miha Čekada, Etienne Hodille, et al.

Journal of Nuclear Materials 591 (2024) 154924

Contents lists available at ScienceDirect

Journal of Nuclear Materials

journal homepage: www.elsevier.com/locate/jnucmat

LIBS analysis of tritium in thin film-type samples

Aurélien Favre [a], Arnaud Bultel [a,*], Mickael Payet [b], Stéphane Vartanian [c], Sébastien Garcia-Argote [b], Vincent Morel [a], Elodie Bernard [c], Sabina Markelj [e], Miha Čekada [e], Etienne Hodille [c], Alexandre Semerok [d], Christian Grisolia [c]

[a] CORIA, UMR 6614, CNRS, University and INSA Rouen-Normandie, 76801 Saint-Etienne du Rouvray Cedex, France
[b] SCBM, CEA Saclay, 91191 Gif-sur-Yvette, France
[c] IRFM, CEA Cadarache, 13801 Saint-Paul-lez-Durance, France
[d] SEARS, CEA Saclay, 91191 Gif-sur-Yvette, France
[e] Jožef Stefan Institute, 1000 Ljubljana, Slovenia

ARTICLE INFO

Keywords:
Tritium
Laser-induced breakdown spectroscopy
LIBS
Quantification

ABSTRACT

Evaluating the mole fraction of hydrogen isotopes in a solid is a difficult task. Few methods allow it to be achieved. LIBS is a laser method based on the electronic excitation of elements and the spontaneous emission of characteristic optical lines. On a sample containing hydrogen isotopes, α-type lines can allow the estimate of their total mole fraction. In addition, LIBS is a discriminating method because it can separate the contributions of isotopes. This paper reports the implementation of this method on thin film-type samples containing hydrogen and tritium.

They consist of nanometric layers of palladium and titanium on a silicon substrate. Under irradiation of nanosecond laser pulses reaching a fluence of the order of 200 J cm^{-2}, LIBS was performed in argon at atmospheric pressure. A detailed spectroscopic study is performed around the T_α line of wavelength 656.039 nm of the Balmer series ($n = 3 \rightarrow 2$) of tritium. An analysis based on the reconstruction of the spectrum under conditions of local thermodynamic equilibrium is carried out. This leads to the estimate of the tritium mole fraction.

1. Introduction

There are still many scientific and technical questions concerning the operation of the ITER reactor. Several of them concerns the penetration of tritium into the plasma facing components (beryllium and tungsten). This penetration results from the significant particle fluxes due to the operating conditions of the machine [1]. It leads to the retention of tritium, which depends on the ageing of the materials [2]. These materials can be pulverised and form deposited layers, which accentuates the trapping of tritium [3] which is then no longer available for fusion reactions. This trapping leads the concerned materials to be radioactive and to the production of helium-3 by radioactive decay [4]. The production of helium-3 can then lead to the embrittlement of the materials [5,6]. After the implementation of tritium [7], the materials concerned must be treated if the total quantity of tritium inside the wall reaches 700 g [3]. This has a significant impact in terms of safety for the technicians in charge [8].

In this context, it is essential to have efficient and flexible means to make the tritium inventory at different locations on the walls in the tokamak. For about fifteen years now [9], the LIBS (Laser-Induced Breakdown Spectroscopy) technique has been seriously considered. It is based on the laser-matter interaction allowing to obtain a plasma from the material to be characterized, which is then the object of a spectroscopic analysis [10]. This technique is now commonly used for the characterisation of alloys [11] but remains under development for the determination of the concentration of light elements in heavy metal matrices [12]. Two methods are used. The first stands on a simple comparison between the spectra obtained from known reference samples in terms of composition and those obtained with the sample to be characterized [13]. The second (calibration-free) method consists in re-

* Corresponding author.
E-mail address: aurelien.favre@coria.fr (A. Favre).
URL: http://www.coria.fr (A. Favre).

https://doi.org/10.1016/j.jnucmat.2024.154924
Received 2 August 2023; Received in revised form 3 November 2023; Accepted 13 January 2024
Available online 18 January 2024

nouncing to the use of these reference samples and in proceeding to the direct analysis of the spectra with the resolution of the radiative transfer equation to get the composition [14]. In a tokamak where strong discrepancies exist locally, it is clear that the first method cannot be implemented and only the second method seems to be applicable.

A number of LIBS tests have been carried out on metal samples containing deuterium [15]. As far as we know, no work has yet been reported exclusively on tritium. It is nevertheless essential to perform tests on tritiated samples. The present paper reports a LIBS analysis of a metallic material containing tritium.

In the following, the different steps leading to this analysis are successively discussed. Due to the radiotoxicity of tritium, a removable LIBS platform with a sealed chamber was developed and characterized. It was then transported to the site able to manage tritiated samples, the Saclay tritium laboratory of the CEA. These samples were prepared according to a particular protocol allowing a high concentration. The laser experiments led to the observation of spectra where the T_α line appears unambiguously. Bursts of successive shots at the same location were also carried out in order to obtain information on the concentration gradients. For comparison, an identical sample not loaded with tritium has been irradiated with laser under the same conditions. Finally, all the spectra obtained were reconstructed using our MERLIN spectra calculation program based on the resolution of the radiative transfer equation [16]. These steps provide quantitative information on the tritium content of the samples.

2. Experimental preparation

2.1. LIBS3H platform

The LIBS technique is based on the laser-matter interaction which results in the ablation of a small portion of the sample [17]. The ablated material is found in the form of gas and dust that can redeposit on the sample [18]. If precautions are not taken when analyzing tritiated samples, the environment may become contaminated. These samples should therefore be kept in a closed chamber to contain the tritium contamination especially the dust one generated during the laser-matter interaction. A 200 cm^3 chamber has been constructed for this purpose. It is cylindrical and has windows for optical viewing and visual control. The main window is located 8 cm from the bottom where the sample is located and transmits the laser pulses. This sealed chamber can be cleaned with acids and solvents after LIBS experiments to dissolve the tritiated dust. During these experiments, it is swept with high purity argon (less than 0.5 ppm of residual H_2 + H_2O) at a flow rate of the order of some 0.1 L min^{-1} at normal pressure: the laser-induced plasma is then very close to LTE (local thermodynamic equilibrium) during most of its expansion and its spectral radiance increases [19,20].

The chamber is positioned on the main optical axis of the platform (see Fig. 1). The optical assembly consists of four lenses. The two lenses L_1 and L_2 allow to extend the diameter of the beam produced by the pulsed laser source before focusing by the lens L_0 on the sample placed at the bottom of the chamber. This allows the irradiance on the sample to be increased at fixed energy. The use of a beamsplitter allows the collection along the main optical axis of the light emitted by the laser-induced plasma. The collected light is sent to an optical fiber after focusing by the L_3 lens which carries the photons to the spectrometer equipped with an emiCCD camera for analysis. The optical elements are contained in a retractable opaque box placed on mini-switches connected to an interlock driving the laser source to avoid any accident.

The main optical element is the beamsplitter. It allows the transmission of laser pulses and the reflection of the light to be analysed. The latter is reduced to the spectral range concerned by the α lines of the Balmer series, which corresponds to the most easily observable transition in the visible at low mole fraction of hydrogen and its isotopes in the laser-induced plasma. Indeed, these lines in the visible spectral range correspond to maximum Einstein coefficients for the spontaneous emission and to the most populated upper levels of the transitions because they are the lowest in energy [21]. The laser source must therefore emit light in a different range. Its choice results from a compromise.

The available energy of the Nd:YAG sources used repeatedly for LIBS experiments decreases as the wavelength decreases. On the other hand, the ablation rate (ablated depth per shot) noted r is generally lower at shorter wavelengths. In order to observe high radiance lines while reducing the impact of the laser-matter interaction on the material, we have chosen to work with laser pulses at $\lambda_L = 532$ nm. The laser source used has a frequency of 10 Hz. The pulse duration is $\tau_L = 6.9$ ns. The quality factor of this source is $M^2 = 16.4$. It is therefore not Gaussian. Fig. 2 illustrates the irradiance distribution imposed by this source, after the L_0 lens of the setup in Fig. 1. It can be seen that this distribution is quite close to a very homogeneous top-hat distribution in the centre without any irradiance peak. The energy delivered per pulse after L_0 is $E_L = 25$ mJ and the average irradiance over the diameter $d_L = 110$ µm of the laser spot on the sample is $\varphi_L = 3.7 \times 10^{14}$ W m^{-2} according to a mean fluence of $F_L = 260$ J cm^{-2}. The Rayleigh distance is $Z_R =$ 1.7 cm so the positioning of the sample with respect to the lens does not need to be very precise. The fluctuations of this laser source are of the order of $\Delta E_L/E_L = 0.1\%$ when the source is hot. Thanks to the shutter placed on the optical axis, the source can operate continuously without irradiating the sample, the laser-matter interaction taking place on the aperture control of this shutter.

Table 1 gathers the data related to the LIBS3H platform.

Prior to experiments, the LIBS3H platform is calibrated using a tungsten ribbon lamp previously characterized by a certified pyrometer with an uncertainty of $\sim$ 40 K ($\pm$ 20 K corresponding to $\pm$ 8% in terms of spectral radiance at 650 nm).

2.2. Samples

- *Experimental conditions*
  Samples were designed in agreement with safety conditions to handle. It means ability to handle for the measurement with the LIBS3H platform and stability of the sample with no degassing at room temperature. The labelling phase of the sample were performed in a dedicated setup for the hydrogen isotope gas phase loading in a similar manner whatever the chosen isotope (^1H, ^2H or ^3H) in the tritium laboratory from CEA-Paris Saclay. The protocol used is divided in three steps. In the first step, the sample is exposed to a H_2 atmosphere (99.9992%) at (573 $\pm$ 2) K and $(1.55 \pm 0.05) \times 10^5$ Pa. During this step, the uptake of hydrogen into the titanium bulk is initialized. Palladium prevents the formation of titanium oxide acting like a barrier for hydrogen isotope absorption. Moreover, traces of water are removed thanks to a cold trap at 194.1 K. In the second step, the sample is exposed to the labelling isotope (^2H or ^3H at 99% of isotopic enrichment) gas atmosphere in a sealed glass tube. The treatment lasts 1 hour for deuterium at (573 $\pm$ 2) K and $(1.55 \pm 0.05) \times 10^5$ Pa. The last step is the air exposure of the sample during one week before measurement. This permits to remove the labile part of the sample. For the tritium samples, a final step is applied. The samples are exposed to an air flow at 30 L/min and 373 K for 1 hour.
- *Hydrogen isotope uptake*
  As several metals, palladium and titanium could form hydrides depending on pressure and temperature conditions [22–24]. The metallic phase noted α can dissolve low amount of hydrogen atom at room temperature in both cases Pd or Ti (below 0.01% at.). However, stable hydride phase could contain, at room temperature, more than 50% at. Increasing the temperature to 573 K enhances the solubilities of the α phases. The used protocol aims at forming hydride-phase of Ti, which is rich in H isotope and stable at room temperature. Finally, the deuterium atomic fraction in the titanium matrix was assessed to 55% by nuclear reaction analysis. For simi-

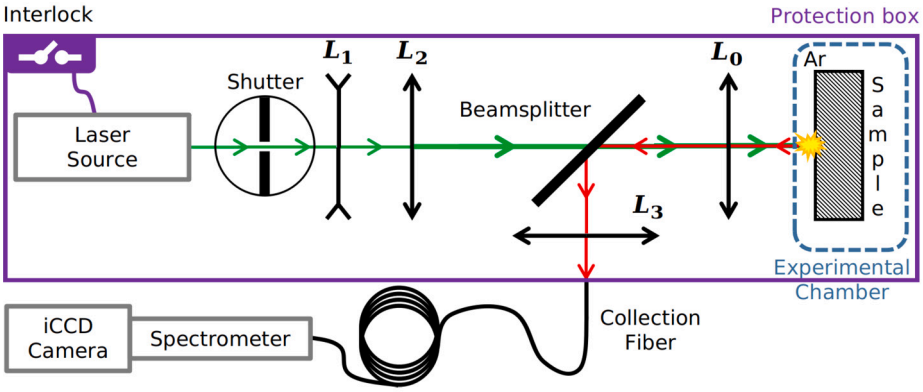

Fig. 1. Schematic view of the LIBS3H platform. The beam from the laser source (green figure) is extended by the lenses L_1 and L_2, passes through the beamsplitter and then through the lens L_0 which focuses it on the sample placed in the experimental chamber. The laser-induced plasma (in yellow) emits light: the red part reflected on the beamsplitter is focused by the L_3 lens on the entrance of the optical fiber towards the spectrometer for analysis. (For interpretation of the colours in the figure(s), the reader is referred to the web version of this article.)

Table 1
Characteristics of the LIBS3H platform.

Optical element	Data	Symbol	Value
ULTRA CFR QUANTEL laser source	Pulse wavelength	λ_L	532 nm
	Energy	E_L	30 mJ
	Pulse duration	τ_L	6.9 ns
	Repetition rate	ν	10 Hz
	Quality factor	M^2	16.4
	Pulse-to-pulse stability	$\Delta E_L/E_L$	0.1%
L_0	Focal length	f_0	100 mm
L_1		f_1	- 50 mm
L_2		f_2	200 mm
L_3		f_3	75 mm
ROPER SCT-320 spectrometer	Focal length	f_s	320 mm
	Aperture	$f_s/4.6$	
	Grating	G	2400 g mm^{-1}
	Optical fiber diameter	d_s	200 µm
PI-MAX HBf camera (1024×1024 pixels)	Pixel sensitive surface		13×13 µm^2
	Quantum efficiency at 650 nm	η	37%

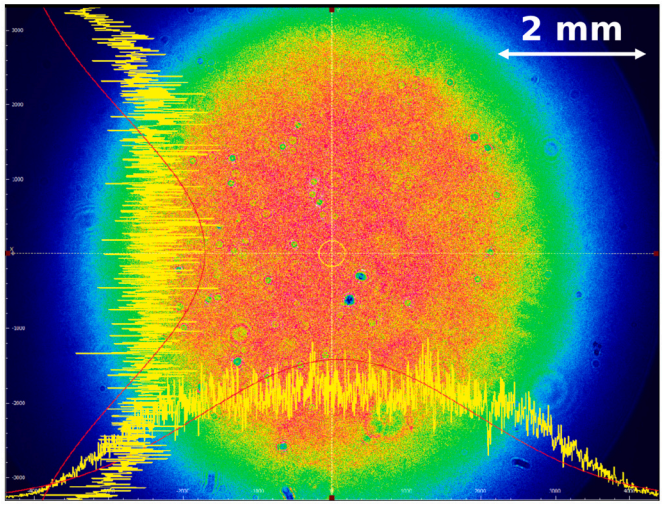

Fig. 2. Image of the laser irradiance distribution ~ 30 mm after the lens L_0. The yellow lines stand for the profile along the vertical and horizontal axes, the red lines for a Gaussian interpolation.

lar tritium sample, the tritium atomic fraction was assessed at 53% using desorption at 1073 K. As the solubility of hydrogen is below 1 ppm [25], it is assumed that the main content remains in the Ti layer. However the cooling down to 293 K in a pure hydrogen isotope gas can lead to a significant part of dissolved species in the thin Pd layer.

For experimental reason, the second step was modified for the Pd-Ti/T-Si sample. The sample was exposed 64 hours at (573 ± 2) K and $(1.17 \pm 0.05) \times 10^5$ Pa. This lower loading pressure would probably not affect the sample content because the hydrogen isotope atomic fraction in the titanium depends on the titanium/palladium interface. Moreover, a longer exposure time could affect the diffusion in the silicon matrix.

- *Diffusion in the sample*

If the temperature is high to form the titanium hydride, the diffusion of hydrogen isotopes at the concerned temperature plays a significant role. At 573 K, Pd hydride could not form below 2×10^5 Pa but the diffusion through the layer is improved compared to 293 K and can supply the formation of titanium hydride. For H diffusion in Pd, the data of Santandrea et al. [26] are used over the range of 273-1273 K according to Birnbaum et al. [27]. At 293 K, nanometric thin layers of Pd have a very low diffusion coefficient [28]. For H diffusion in Ti, the data of Lu et al. [28] are used over the range of 323-1073 K. For H diffusion in Si (single crystal), the data of Ichimiya et al. [29] have been determined over the range 673-773 K. They can be extended to from 323 to 973 K interval according to Pearton et al. [30] and similar to those for the diffusion of T according to the same authors. For T diffusion in Pd, the data of Buchold & Sicking [31] are used at 293 K. If a

Table 2
Characteristics of the diffusion process of H and T within Pd, Ti and Si at 293 K for $\tau_d = 64$ hour.

Material X	Diffusion of H at 293 K			Diffusion of T at 293 K		
	$D_{H,X}$ ($m^2\ s^{-1}$)	Ref.	$\delta_{H,X}$ (m)	$D_{T,X}$ ($m^2\ s^{-1}$)	Ref.	$\delta_{T,X}$ (m)
Pd	2×10^{-15}	(thin layer [44])	2.1×10^{-5}	1.9×10^{-11}	[31]	2.1×10^{-3}
Ti	1.6×10^{-15}	[28]	1.9×10^{-5}	2.0×10^{-15}	[28]	2.1×10^{-5}
Si	8.0×10^{-19}	[29,30]	4.3×10^{-7}	8.0×10^{-19}	[29,30]	4.3×10^{-7}

Table 3
Characteristics of the diffusion process of H and T within Pd, Ti and Si at 573 K for $\tau_d =$ 64 hour.

Material X	Diffusion of H at 573 K			Diffusion of T at 573 K		
	$D_{H,X}$ ($m^2\ s^{-1}$)	Ref.	$\delta_{H,X}$ (m)	$D_{T,X}$ ($m^2\ s^{-1}$)	Ref.	$\delta_{T,X}$ (m)
Pd	2.9×10^{-9}	[26,27]	2.6×10^{-2}	2.9×10^{-9}	[26,27]	2.6×10^{-2}
Ti	4.3×10^{-11}	[28]	3.1×10^{-3}	3.4×10^{-11}	[28]	2.8×10^{-3}
Si	5.1×10^{-14}	[29,30]	1.1×10^{-4}	5.1×10^{-14}	[29,30]	1.1×10^{-4}

difference should be expected concerning the diffusion of each hydrogen isotope due to their different mass, the diffusion coefficient could be supposed equivalent in a first approximation. The diffusion is much more influenced by the difference of the substrate (Pd, Ti, or Si), and their present defects. These data are summarized in the Tables 2 and 3. To compare the orders of magnitude of the diffusion of Y within X, it is relevant to use the characteristic diffusion length $\delta_{Y,X}$ defined by the relation between the diffusion coefficient $D_{Y,X}$ and the time of diffusion τ_d

$$\delta_{Y,X} = \sqrt{D_{Y,X}\,\tau_d} \tag{1}$$

The retained diffusion time is fixed to the 64 hours required by the uptake tritium process. Tables 2 and 3 show that Pd and Ti layers are too thin to limit the diffusion into Si and that the diffusion within the Si substrate significant.

- *Hydrogen isotope in the silicon*
  No specific measurement was performed to estimate the hydrogen isotope content in the silicon matrix but regarding some studies, hydrogen can diffuse through Si [25,32–35]. During the absorption phase, hydrogen isotope can reach the Ti/Si interface and could interact with the Si substrate. At 573 K, hydrogen diffuses into Si in atomic form as interstitial [33]. In the usual experiments designed to measure hydrogen diffusion in single crystal silicon, the atom density is low because the source is (1) a low pressure hydrogen plasma, or (2) molecular hydrogen directly interacting with the surface (so-called infusion experiments). The density of atoms on the surface is then in case (2) conditioned by the dissociative adsorption of H_2 [34], which leads to low densities similar to case (1). In case (1) or (2), the density of atoms on the surface is then typically 10^{21} m^{-3} [29], 10^{24} m^{-3} [35], 10^{25} m^{-3} [35,37], 10^{26} m^{-3} [38–41], 10^{27} m^{-3} [36,42,43]. In the present case, the presence of the titanium layer containing a density of the order of 10^{28} m^{-3} hydrogen atoms provides a sufficient source for diffusion into the silicon layer. Indeed, the strong tendency to form Si-H bonds means that silicon can be strongly charged with hydrogen [36].

The analysis by LIBS has permitted to investigate the high hydrogen isotope content from the Pd/Ti layers but also the traces present in the silicon substrate. In order to carry out spectral comparisons, other samples were irradiated. These samples were titanium samples (TA6V type) and a silicon wafer. All the samples studied in this paper are listed in Table 4.

3. Results

3.1. Impact of laser-matter interaction on the sample

The surface of the Pd-Ti-Si and Pd-Ti/D-Si samples has been observed by scanning electron microscopy. It consists of a fairly regular paving based on about 30 μm×30 μm squares. When the laser-matter interaction occurs, the surface is modified. This can be seen on Fig. 3 where between 1 and 10 shots were fired at the same location on the samples. A circle of material about $d_m = 200$ μm in diameter is formed from the first shot. Its height increases from shot to shot. After 5 shots, this height is about 10 μm and it is about 20 μm after 10 shots. In the centre, a small dome forms with similar heights. These formations are neither due to the diameter of the laser spot on the sample (we observe that $d_L < d_m$), nor to a defect of uniformity of the irradiance distribution (see section 2.1).

Fig. 4 displays details. From the first shot, we can see the smoothing of the asperities of the paving mentioned above. As the number of shots increases, a solidified layer is formed, forming characteristic folds on the periphery. This is the sign of a solid → liquid phase change usual for laser-matter interaction at the nanosecond scale [45]. At the edge of this solidified sheet, Fig. 5 shows that the structure of the material is different depending on the nature of the sample. Since the two images in Fig. 5 differ in deuterium charge, we conclude that the sample is indeed modified by the charge and that this modification leads to the modification of the laser-matter interaction.

3.2. Ablation rate estimate

The palladium and titanium layers are a few tens of nm thick, which is quite small. To allow a profilometric measurement, the ablation rate r must be low. Low spectral radiance is expected, as it is proportional to the ablated mass as a first approximation. In order to estimate this ablation rate, the spectroscopic observation conditions must be optimised.

According to the spectroscopic tables [21,46–48], palladium does not emit any atomic or ionic lines in the range [653, 659] nm where the α lines of the Balmer series of hydrogen isotopes can be observed. The spectrum of palladium is rather rich in the UV. In particular, the line at 340.458 nm has an Einstein coefficient of spontaneous emission greater than 10^8 s^{-1} and an upper level of the associated transition at about 4.5 eV. Titanium emits readily in the [653, 659] nm range. Silicon does not emit in this range. In the UV, its spectrum is also quite rich. The line at 288.158 nm has similar characteristics to palladium. Table 5 gathers these lines.

We carried out test shots at the same location on a virgin sample (neither thermal preparation nor tritiation, Pd-Ti-Si samples) under the

Table 4
Studied samples.

Label	Composition (along the pulse propagation)	Thickness (nm)	Preparation
Pd-Ti-Si	Palladium Titanium Silicon	16 55 ∞ (wafer)	Sputtering of Pd target Sputtering of Ti target Industrial
Pd-Ti/D-Si	Palladium Titanium + Deuterium Silicon	16 55 ∞ (wafer)	Sputtering of Pd target Sputtering of Ti target Industrial
Pd-Ti/T-Si	Palladium Titanium + Tritium Silicon	16 55 ∞ (wafer)	Sputtering of Pd target Sputtering of Ti target Industrial
Ti-Al-V	Ti (90 w%, 86.2 mol%) + Al (6 w%, 10.2 mol%) + V (4 w%, 3.6 mol%)	∞ (metal)	Industrial (TA6V)
Si	Silicon	∞ (wafer)	Industrial

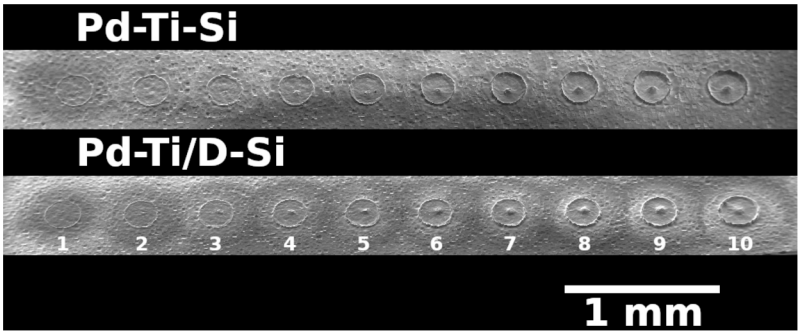

Fig. 3. Evolution of the crater for 1 to 10 shots performed at the same location for the Pd-Ti-Si (top) and the Pd-Ti/D-Si (bottom) samples.

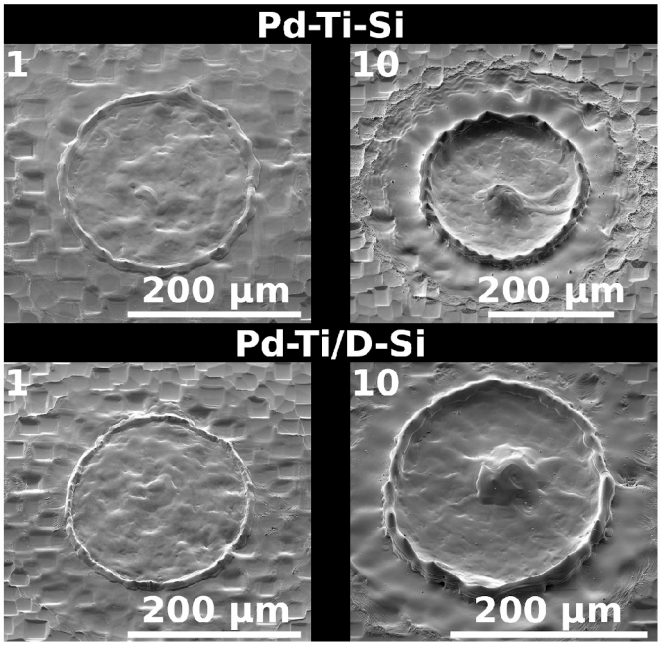

Fig. 4. Aspect of the crater for 1 (left) and 10 (right) shots performed at the same location for the Pd-Ti-Si (top) and the Pd-Ti/D-Si (bottom) samples.

nominal irradiance conditions. In the following, the gate-delay t is measured with respect to the time when the laser pulse reaches the sample and the gate width Δt corresponds to the recording time of the signal. Thus, when $(t, \Delta t)$ is given, the signal is accumulated during the time interval $[t, t + \Delta t]$. The measurements were performed under the conditions $(t, \Delta t) = (10, 2)$ µs (see section 3.3).

The lines of Table 5 are easily observed. Fig. 6 shows the evolution of their spectral radiance at the centre of the line with respect to that observed at the first pulse $\frac{L_\lambda}{L_{\lambda_0}}$ as a function of the shot number n_p. No uncertainty is estimated, the discussion being qualitative. It is important to mention that the silicon line is observed from the first shot, which indicates that the average ablation rate exceeds the value of the cumulative thickness of the palladium and titanium layers. It can therefore be stated that

$$r_{min} > z_{Pd} + z_{Ti} \sim 80 \text{ nm} \tag{2}$$

This observation is consistent with the fact that the radiance level of the titanium lines also undergoes a continuous decrease. If the average ablation rate had been lower than the depth of the titanium layer, the signal would have increased during the second pulse. This conclusion is supported by the results of the work of Torrisi et al. [49] on palladium, of Reimers et al. [50] on titanium and of the review by Schutz et al. [51] on silicon.

Let us analyse in detail the laser-matter interaction from one layer to the other. The characteristic absorption length of palladium is the inverse of the light absorption coefficient α_{Pd} which is related to the complex part k_{Pd} of the refractive index by [52]

$$\alpha_{Pd} = \frac{4\pi k_{Pd}}{\lambda_L} \tag{3}$$

Avila et al. [53] have measured the influence of low hydrogen absorption on this complex part in the optical range [400, 900] nm of a 10 nm thick palladium thin layer. They showed that its value is reduced from 20% at 532 nm at room temperature, i.e. when the hydrogen absorption is not optimised. This leads to an increase in the characteristic absorp-

Table 5
Spectral database.

Line	Transition $i \leftarrow k$	λ (nm)	A_{ki} (s^{-1})	g_i - g_k	E_i (eV) - E_k (eV)	Ref.
H_α	$(2p^2P^o+2s^2S)$ - $(3p^2P^o+3s^2S+3d^2D)$	656.283	4.41×10^7	8 - 18	10.199 - 12.088	[48]
T_α	$(2p^2P^o+2s^2S)$ - $(3p^2P^o+3s^2S+3d^2D)$	656.039	4.41×10^7	8 - 18	10.203 - 12.092	[48]
Pd I	$4d^9(^2D_{5/2})5s^2[5/2]$ - $4d^9(^2D_{5/2})5p^2[7/2]^o$	340.458	1.34×10^8	7 - 9	0.814 - 4.454	[21]
Si I	$3s^23p^2\ ^1D$ - $3s^23p4s\ ^1P^o$	288.158	2.17×10^8	5 - 3	0.781 - 5.082	[21]
Ti I	$(^4F)4p\ y^5G$ - $(^4F)4d\ e^5H$	653.642	1.74×10^6	13 - 15	3.337 - 5.233	[46]
Ti I	$(^4F)4p\ y^5F$ - $(^4F)4d\ ^5F$	654.304	1.62×10^7	3 - 3	3.545 - 5.440	[46]
Ti I	$(^4F)4s\ b^3F$ - $(^1D)sp\ x^3F$	654.627	1.41×10^6	5 - 5	1.430 - 3.323	[46]
Ti I	$(^4F)4p\ y^5F$ - $(^4F)4d\ ^5F$	654.833	1.76×10^7	7 - 7	3.559 - 5.452	[46]
Ti I	$(^4F)4s\ b^3F$ - $(^1D)sp\ x^3F$	655.422	1.34×10^6	7 - 7	1.443 - 3.334	[21], [46]
Ti II	$(^3F)4d\ ^2P$ - $(^3F)4f\ ^4P$	655.564	7.49×10^6	4 - 2	8.281 - 10.172	[46]
Ti I	$(^4F)4s\ b^3F$ - $(^1D)sp\ x^3F$	655.606	1.45×10^6	9 - 9	1.460 - 3.351	[21], [46]
Ti II	$(^3P)4s\ b^2P$ - $(^3F)4p\ z^2D$	655.959	3.71×10^5	2 - 4	2.048 - 3.937	[46]
Ti II	$(^3F)4d\ ^2P$ - $(^3F)4f\ ^4P$	656.550	3.93×10^6	4 - 4	8.281 - 10.169	[46]
Ti I	$(^4F)4p\ y^5F$ - $(^4F)4d\ f^5F$	656.550	2.30×10^7	11 - 11	3.583 - 5.471	[46]
Ti I	$(^4F)4p\ y^5F$ - $(^4F)4d\ ^5F$	657.226	7.12×10^6	7 - 5	3.559 - 5.445	[46]
Ti I	$(^2H)4s\ a^1H$ - $(^1G)sp\ y^1G$	657.516	2.18×10^6	11 - 9	2.578 - 4.463	[46]
Ti I	$(^1D)sp\ x^3F$ - $(^4F)4d\ e^3H$	658.185	1.24×10^6	9 - 9	3.351 - 5.234	[46]
Ti I	$(^4F)4p\ y^5F$ - $(^4F)4d\ ^5F$	658.525	5.08×10^6	9 - 7	3.569 - 5.452	[46]
V I	$d^3s^2\ a^4P$ - $(^5D)4p\ z^4P$	653.142	3.77×10^6	6 - 6	1.218 - 3.116	[46]

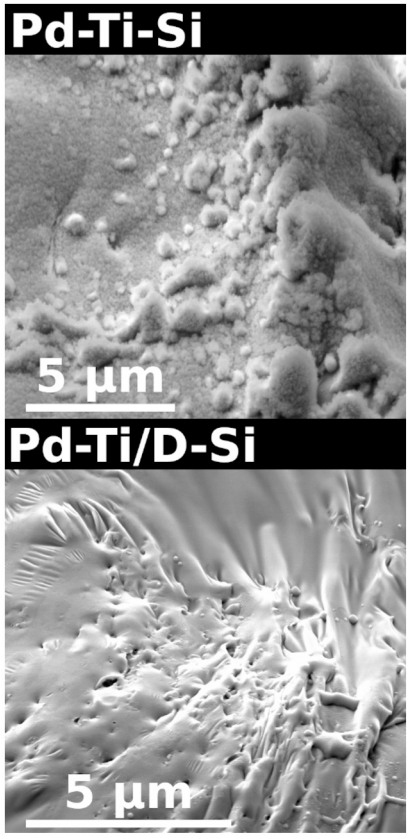

Fig. 5. Structure of the external border of the crater beyond the circular enhancement, around 200 µm from the centre.

tion length to 15 nm ($k_{Pd} = 2.9$). A stronger increase can be expected as the hydrogen mole fraction increases. This results in the palladium layer optically attenuating the laser irradiance by about 60%. The optical properties of hydrogenated titanium have been studied by Palm et al. [54]. The progressive increase in the amount of hydrogen contained in titanium leads to a decrease in the real part ϵ_1 and an increase in the imaginary part ϵ_2 of the dielectric function. The temperature increase only influences ϵ_2 at 532 nm. Their results lead to $k_{Ti} \sim 1,7$, which leads to a value of the characteristic absorption length of the order of 25 nm. The absorption of the pulse takes place in the Pd-Ti thin layers since the irradiance at the Ti-Si interface is only

$$\frac{\varphi\left(z_{Pd} + z_{Ti}\right)}{\varphi_L} = e^{-\left(\alpha_{Pd} z_{Pd} + \alpha_{Ti} z_{Ti}\right)} \sim 0.03 \tag{4}$$

The silicon beyond this point absorbs the rest of the pulse. The characteristic absorption length at 532 nm is 1 µm according to Bucher et al. [55]. This small amount of energy little contributes to the production of the observed plasma and serves rather to preheat the silicon submitted to the diffusion of the thermal energy deposited in the Pd and Ti layers. This diffusion takes place over the characteristic length

$$z_{Si} \sim \sqrt{a_{Si}\,\tau_L} \tag{5}$$

similar to equation (1) where a_{Si} is the thermal diffusivity of silicon. Yamamoto et al. [56] have shown that a_{Si} depends little on the temperature above 800 K in both the solid and liquid states. The obtained value $a_{Si} \sim 2 \times 10^{-5}$ m^2 s^{-1} leads to $z_{Si} \sim 380$ nm. The depth of the crater, i.e. the ablation rate, is therefore close to z_{Si}. Note that this rate is lower than the ablated depth on silicon at 532 nm for fluences of the order of 10 J cm^{-2}, which corresponds globally to $0.03 \times F_L$ according to Schutz et al. [51]. This is logical because in the present case the energy is preferentially dissipated in the Pd-Ti thin layers and not in the silicon, as a direct experiment on Si would require for the measurement of its ablation rate. The value of z_{Si} is very large compared to the thickness of the Pd-Ti thin films. The energy deposition therefore takes place in the Pd-Ti thin layers, but the ablation takes place preferentially in the silicon. The hydrogen and tritium observed in the spectra will not only be due to their presence in these layers but also to these species having diffused into the silicon since $\delta_{H,Si} > z_{Si}$ and $\delta_{T,Si} > z_{Si}$.

Regarding Fig. 6, the results seem to be consistent with an exponential decay of the type

$$\frac{L_\lambda}{L_{\lambda_0}} = e^{-(n_p-1)/n_{r,\lambda}} \tag{6}$$

In equation (6), $n_{r,\lambda}$ is the number of pulses characteristic of the decay of the signal at wavelength λ. We have $n_{r,340.458} = 0.7$, $n_{r,654.304} = 0.9$, $n_{r,654.627} = 1.1$ and $n_{r,657.516} = 1.2$. Thus, on average, $n_r = 1$ characteristic pulse is obtained. This means that after 3 pulses, the signal has lost its order of magnitude at the first pulse. As the pulses show a rather slow radial decrease of the irradiance at the periphery (cf. 2.1), the residual signal is then only due to the inefficient ablation still taking place at the periphery of the pulse.

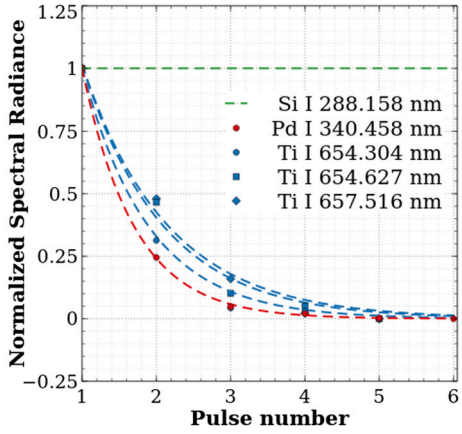

Fig. 6. Evolution of the central line normalized spectral radiance with respect to the first one for the lines in part listed in Table 5. The dashed lines refer to the exponential interpolation.

3.3. Emission of Si, Ti-Al-V, Pd-Ti-Si and Pd-Ti/T-Si

The acquisition conditions have been chosen to reduce the LTE departure of the laser-induced plasma. The value of the gate delay must therefore be low so that the recombination does not lower the electron density too much. Conversely, the plasma must have time to recombine so that the Stark broadening of the emitted lines is low, in particular that of the hydrogen isotope lines. A satisfactory spectral resolution is then obtained. But the radiance of these lines is then reduced. As a shot after shot observation is necessary due to the small layers thickness of the samples studied, a fairly long gate width is required. After several tests, a gate delay of 10 μs and a gate width of 2 μs have been considered as satisfactory. These conditions are very close to the ones adopted by Eseller et al. [57] for the LIBS diagnosis of hydrogen in the gas phase. They are also close to the conditions adopted by Almaviva et al. [58] for the measurement of H and D in tungsten samples for which the gate delay is of the order of several μs. The configuration is a bit different here because the presence of a tungsten line at 656.320 nm interferes with the α lines of hydrogen isotopes. Marin Roldan et al. [59] have carried out LIBS measurements (under argon) of the composition of samples made of tungsten and zirconium loaded with deuterium. Here too, the gate delay is of the order of several μs, as is the gate width, in order to achieve sufficient spectral resolution. A study by Gaviola et al. [60] focuses on LIBS measurements of deuterium in titanium. Unfortunately, no information is reported on the gate delay and gate width values. A study by Man [61] reports the evolution of the spectrum of a titanium plasma obtained in air under conditions close to our own. After a sharp drop in the intensity of the initial recombination continuum typical of all laser-induced plasmas, the intensity of the titanium lines undergoes a rather slow decrease from a gate delay of 800 ns. After 2.5 μs, the intensity of these lines is about divided by a factor of five. Moreover, the decrease in the electron temperature is also slow around 6000-8000 K. These evolutions and values are also observed for silicon plasmas [62,63]. In any case, the chosen gate delay value exceeds the instant from which the evolutions of the plasma parameters are slow and the electron density is still important. The measurements reported in the following have therefore been carried out under the conditions $(t, \Delta t) = (10, 2)$ μs.

In order to clearly demonstrate the contribution of tritium to the observed spectra over the spectral range of interest [653, 659] nm, reference spectra were measured on a Si sample, a Ti-Al-V sample [TA6V of composition Ti (90 w%, 86. 2 mol%), Al (6 w%, 10.2 mol%), V (4 w%, 3.6 mol%)], a Pd-Ti-Si sample and a Pd-Ti/T-Si sample (see Table 4). Fig. 7 illustrates the spectra obtained. The uncertainty due to the conversion process from the signal level to the spectral radiance corresponds to about ± 9% of the final spectral radiance. This value results

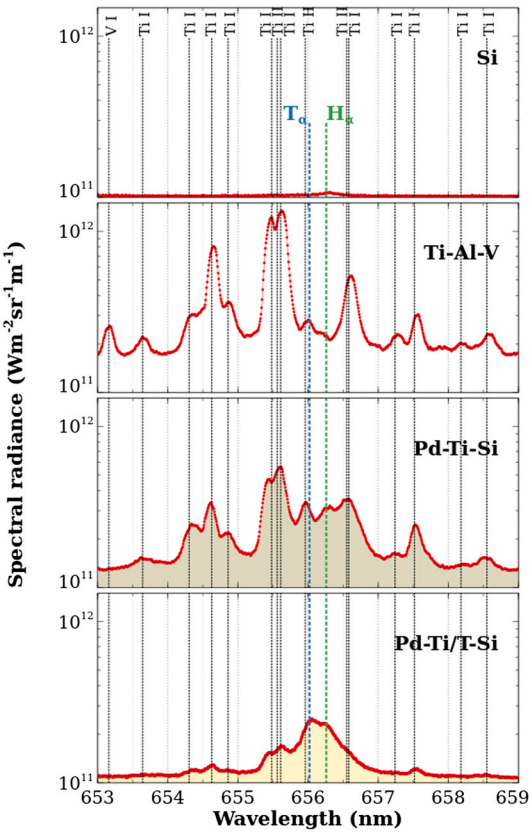

Fig. 7. Spectra observed on the range [653, 659] nm resulting from one single pulse delivered on the samples Si, Ti-Al-V, Pd-Ti-Si and Pd-Ti/T-Si using the LIBS3H platform in argon in the gate conditions $(t, \Delta t) = (10, 2)$ μs.

from the calibration uncertainty of the pyrometer used to measure the spectral radiance of the tungsten ribbon lamp at 650 nm (40 K corresponding to ± 8% of the spectral radiance) and to the setting precision on the power supply driving the ribbon lamp current (with the contribution of ± 1%).

1. *Si sample*
   No silicon lines appear in the spectrum. Only the H_α line is observed. This very weak line is due to the residual presence of hydrogen in the high purity ambient argon filling the experimental chamber.
2. *Ti-Al-V sample*
   This very small contribution can be seen in the Ti-Al-V spectrum. However, most of the spectrum is due to Ti I transitions (see Table 5). It is interesting to note that a low intensity Ti II transition appears in the spectrum at 655.959 nm. The observation of this line is a sign of a significant ionization rate. However, it has a low intensity, which suggests a low value of electron density confirmed by the Stark broadening of the lines, which does not exceed 0.25 nm. There is also a contribution to the spectrum from a vanadium line observed at 653.142 nm. This is due to the fact that the sample is in fact commercial TA6V, whose mole fraction of vanadium reaches 3.6%.
3. *Pd-Ti-Si sample*
   Of course, the vanadium line is not observed in the spectrum obtained on this sample. The spectrum has the same feature, although characterized by a lower spectral radiance. This is due to the fact that the amount of ablated titanium is obviously lower, the Pd-Ti-Si sample being a multilayer sample. This spectrum is particularly distinct from that obtained on Ti-Al-V over the range [656.0, 656.5] nm. Indeed, the spectral radiance relative to that of the lines observed around 655.5 nm increases from one sample to

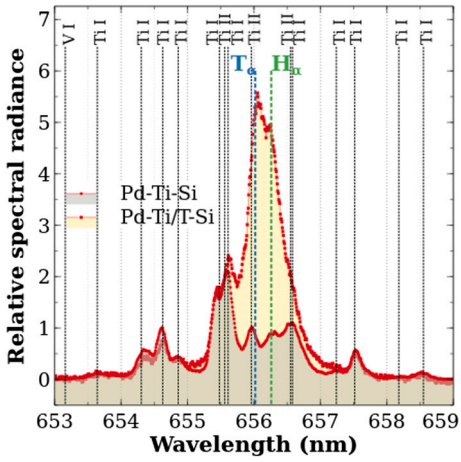

Fig. 8. Normalized spectra observed on the range [653, 659] nm resulting from one single shot delivered on the samples Pd-Ti-Si and Pd-Ti/T-Si using the LIBS3H platform in argon in the gate conditions $(t, \Delta t) = (10, 2)$ µs. The contributions due to the H_α and T_α lines are observed on the interval [655.7, 656.7] nm.

the other, while remaining lower than those of these lines, which are the most intense of all those observed on Fig. 9.

4. *Pd-Ti/T-Si sample*
   The spectrum is weaker than the previous ones. This means that the ablation is performed differently. This time, the spectral interval [656.0, 656.5] nm is characterized by a higher spectral radiance than the lines around 655.5 nm which are always observed. This is due to the contribution of the H_α and T_α lines.

As the decrease in spectral radiance is significant, it is interesting to normalize the obtained spectra. We have chosen to normalize with respect to the spectral radiance observed at 655.4 nm removing the background contribution (cf. Fig. 8). Thus, the spectral radiance of the peak of the Ti I line at 654.833 nm corresponds to unity and that of the Ti I line at 655.483 nm corresponds to 2. With this procedure, the obtained spectra are quite similar, except in the range [655.7, 656.7] nm where the contributions of the H_α and the T_α lines are unambiguously observed.

It can be seen that the peaks of the lines are discernible, even if the Rayleigh criterion is not fulfilled. The distinction between hydrogen and tritium is therefore possible.

3.4. Shot to shot Pd-Ti/T-Si emission

We recorded the spectrum of the next 4 shots obtained in the same crater to see the correlation with Fig. 6. Fig. 9 illustrates the results obtained. It can be seen that the titanium lines disappear from the spectrum in the third shot for which even the Ti I line at 657.516 nm is no longer observable. This is consistent with Fig. 6. On the other hand, the distinction between tritium and hydrogen is still possible. Indeed, the T_α line disappears from the spectrum more quickly than the H_α line.

This disappearance is obvious when the spectra obtained at each laser pulse are normalized to the central spectral radiance of the H_α line. Fig. 10 illustrates this normalization with subtraction of the background contribution. From the second pulse onwards, the contribution to the spectrum of the T_α line becomes smaller than that of the H_α line. Along the pulses series, the tritium signal disappears: it is reasonable to assume that tritium is no longer detectable in the spectrum of the 5th pulse.

By the second pulse, the Ti I line at 656.550 nm no longer contributes to a spectral radiance enhancement on the wing of the H_α line. Fig. 10 also shows that the other titanium lines disappear from the spectrum at the second pulse while the T_α line is still observable,

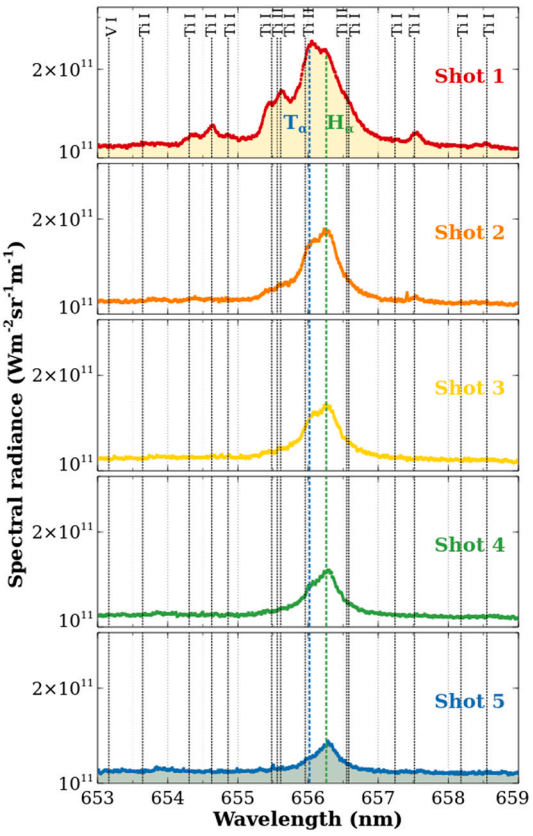

Fig. 9. Spectra observed on the range [653, 659] nm resulting from 5 successive laser pulses delivered at the same location on the sample Pd-Ti/T-Si using the LIBS3H platform in argon in the gate conditions $(t, \Delta t) = (10, 2)$ µs.

although attenuated. This indicates that tritium is present in significant quantities beyond the titanium layer, in the silicon substrate, even if a possible activation of additional diffusion due to the heating following the laser irradiation cannot be excluded. When these lines have disappeared, the H_α line is found to have its wing between 656.3 nm and 656.5 nm almost superimposable from one shot to another. The T_α line does not have sufficient broadening to contribute to the spectral radiance at these wavelengths. This means that the plasma has a constant electron density from one shot to the next for the gate delay and gate width conditions chosen. We also note that the spectral radiance maximum of the H_α line is slightly shifted in wavelength. The electron density of the plasma is indeed sufficient to induce a slight Stark shift $\delta\lambda_{\alpha,S}$. This shift and the broadening of the line at half maximum $\Delta\lambda_{\alpha,S}$ allow an approximate determination of the electron density.

The paper of Gigosos et al. [64] allows us to determine the electron density n_e from the full width at half maximum $\Delta\lambda_{\alpha,S}$ of the H_α line, which can be expressed mathematically by

$$n_e\,[\mathrm{m}^{-3}] = 10^{22}\left(\frac{\Delta\lambda_{\alpha,S}\,[\mathrm{nm}]}{0.252}\right)^{1.67049} \tag{7}$$

On Fig. 10, the full width at half maximum for pulse 5 is estimated to be about 0.22 nm. This gives an approximate value of n_e of the order of 8×10^{21} m^{-3}. The value of the Stark shift is close to 0.02 nm. It is quite approximate due to the low spectral resolution at this scale. The values measured by Buscher et al. [65] at low electron density can be interpolated by the relation

$$n_e\,[\mathrm{m}^{-3}] = 10^{22}\left(\frac{\delta\lambda_{\alpha,S}\,[\mathrm{nm}]}{0.00413}\right)^{0.9128} \tag{8}$$

From the equation (8), we derive a value close to 4×10^{22} m^{-3}. We can conclude that the electron density is $n_e \sim 10^{22}$ m^{-3}.

Table 6
Minimum electron density $n_{e,min}$(X) to obtain a X plasma in LTE at $T_e = 8000$ K according to different authors.

Criterion	Year - Ref.	$n_{e,min}$(Si)	$n_{e,min}$(Ti)	$n_{e,min}$(H-T)	$n_{e,min}$(Ar)
Wilson	1962 - [67]	2.9×10^{24}	1.7×10^{24}	1.4×10^{25}	2.1×10^{25}
Griem	1963 - [68]	1.1×10^{21}	1.1×10^{20}	9.5×10^{21}	1.4×10^{22}
McWhirter	1965 - [69]	1.6×10^{21}	6.4×10^{19}	1.5×10^{23}	2.3×10^{23}
Drawin	1969 - [70]	1.2×10^{20}	1.3×10^{17}	9.9×10^{21}	8.1×10^{22}
Hey	1976 - [71]	9.1×10^{22}	6.9×10^{21}	1.2×10^{24}	1.8×10^{24}
Fujimoto and McWhirter	1990 - [72]		5.5×10^{23}		

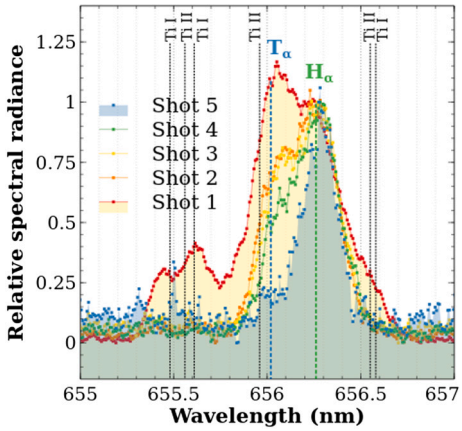

Fig. 10. Normalized spectra observed on the range [655, 657] nm resulting from the successive pulses delivered on the sample Pd-Ti/T-Si using the LIBS3H platform in argon in the gate conditions $(t, \Delta t) = (10, 2)$ µs. The normalization is performed with respect to the H_α line central spectral radiance. The blue area corresponds to the last pulse.

3.5. Departure from LTE discussion

We can verify if the previous order of magnitude is compatible with the LTE of the laser-induced plasma. This can be done indirectly by studying various simple criteria. They give a minimum electron density $n_{e,min}$(X) allowing the plasma of species X to be at LTE. This density is basically derived from simplified expressions of the electron impact excitation cross sections of the species considered and the Einstein coefficients of spontaneous emission. They involve the largest energy difference between two successive excited levels or that related to the $E_2 - E_1$ resonance transition, their degeneracy factor, a Gaunt factor $\langle\bar{g}\rangle$ [66] and the electron temperature T_e. Table 6 gathers the results obtained for this minimum electron density according to Wilson [67], Griem [68], McWhirter [69], Drawin [70], Hey [71] and Fujimoto & McWhirter [72] for plasmas of Si, Ti, H-T and Ar at $T_e = 8000$ K. This temperature level is considered owing to the estimate of T_e performed in section 3.6.2.

These results extend over a fairly wide range for each of the atoms considered. For Ti, it seems that the electron density obtained in the section 3.4 is sufficient. Indeed, only the Wilson and Fujimoto & McWhirter criteria are not fulfilled. For Si, the results are also rather favourable. On the other hand, for H or T, the $n_e \sim 10^{22}$ m^{-3} value obtained in section 3.4 corresponds to the low values listed in Table 6. For Ar, the value $n_e \sim 10^{22}$ m^{-3} is found only for Griem.

Among the previous criteria, two have a special place. Griem's criterion is historical and McWhirter's criterion is now established in the LIBS research community. They are based on similar approaches. The Griem criterion compares the decrease in the number of particles on the fundamental level by electron impact excitation to the first resonant level and the increase in this number by resonant radiation from the same level. The McWhirter criterion does the same thing but generalises this approach to all levels. Mathematically, they exploit approximate (hydrogen-like) analytical forms for excitation cross sections and Einstein coefficients of spontaneous emission. They should therefore not be considered too restrictively. Moreover, these criteria do not take into account self-absorption because no characteristic dimension of the plasma under consideration is involved. This self-absorption reduces the threshold electron density to obtain the LTE. This is discussed in the article by Cristoforetti et al. [73] which specifies after a review that a reduction of a factor of 10 on the threshold indicated by McWhirter can be reasonably considered.

Table 7
Characteristic time and length scales for $n_e = 10^{22}$ m^{-3} and $T_e = 8000$ K according to Drawin [74].

Element	Si	Ti	H, T	Ar
E_1 - E_2 (eV)	0 - 4.930	0 - 2.396	0 - 10.199	0 - 11.624
f_{12}	2.10×10^{-1}	1.70×10^{-2}	4.16×10^{-1}	6.75×10^{-2}
Ψ_1	1.33×10^{-4}	9.34×10^{-3}	1.93×10^{-8}	1.77×10^{-9}
α^{CR} (m^3 s^{-1})		4.10×10^{-17}		
τ_i (s)	2.60×10^{-6}	2.22×10^{-7}	1.87×10^{-2}	1.43×10^{0}
τ_r (s)		2.44×10^{-6}		
τ_p (s)	1.26×10^{-6}	2.04×10^{-7}	2.44×10^{-6}	2.44×10^{-6}
λ_g (m)	2.38×10^{-7}	4.67×10^{-8}	1.46×10^{-4}	1.36×10^{-4}

On the other hand, the value of the gate delay $t = 10$ µs chosen for our experiments is large. It can be compared to the time τ_p needed for the plasma to reach equilibrium while recombining. According to Drawin [74], this characteristic time is related to the characteristic times of ionization τ_i and recombination τ_r of the plasma by

$$\frac{1}{\tau_p} \sim \frac{1}{\tau_i} + \frac{1}{\tau_r} \tag{9}$$

since the plasma is in a quasisteady state. The characteristic ionization time is given by

$$\tau_i \sim \frac{A}{n_e f_{12} \Psi_1\left(\frac{E_2-E_1}{k_B T_e}\right)} \frac{E_2 - E_1}{E_1^H} \sqrt{\frac{k_B T_e}{E_1^H}} \tag{10}$$

and the characteristic recombination time by

$$\tau_r \sim \frac{1}{n_e \alpha^{CR}} \tag{11}$$

in which $A = 8.9\times10^{12}$ s m^{-3}, f_{12} is the absorption oscillator strength of the resonance transition, E_1^H is the ionization energy of the hydrogen atom and α^{CR} is the collisional-radiative recombination coefficient. This coefficient and the Ψ_1 function are given by Drawin [74]. Table 7 gives these characteristic times calculated for the different atoms forming the plasma for an electron density $n_e = 10^{22}$ m^{-3} and an electron temperature $T_e = 8000$ K. It can be seen that τ_p is of the order of a few µs. The choice of a gate delay of $t = 10$ µs is thus favourable to the achievement of LTE.

The plasma expands into the surrounding argon gas at a very high initial velocity. Its expansion speed is hypersonic. Then, as it expands, its internal density gradients relax. In particular, argon and species in the ablated sample diffuse mutually. Around $t = 10$ µs, the plasma radius can easily reach the value $z_p = 1000$ µm. This corresponds to the spatial scale of these gradients. In order to assess the uniformity of the plasma, it is interesting to calculate the characteristic relaxation length λ_g of the inhomogeneities. Using the information provided by

Drawin [74], we have calculated the values of λ_g for the plasma species adopting a relative density deviation of 50% as the uniformity criterion. Table 7 lists the values obtained. It can be seen that z_p exceeds λ_g by a large margin. It is therefore reasonable to assume that the plasma is almost uniform. This conclusion is reinforced by the use of argon as ambient gas. It is indeed known that this gas allows to obtain homogenous laser-induced plasmas [75].

Under these conditions, we can conclude that it is reasonable here to consider the laser-induced plasma under the conditions of the previous sections as being at LTE and uniform. The spectra have therefore been reconstructed using the MERLIN (MultiElemental Radiative equi-LibrIum emissioN) code [16].

3.6. Spectra reconstruction

A uniform LTE plasma of length z_p and temperature T has a spectral radiance driven by

$$L_{\lambda,T} = L^0_{\lambda,T}\left(1 - e^{\alpha_{\lambda,T}\, z_p}\right) \tag{12}$$

where $L^0_{\lambda,T}$ is the spectral radiance of the blackbody and $\alpha_{\lambda,T}$ is the absorption coefficient [76]. This coefficient depends on the set of radiative elementary phenomena that can take place such as

$$\alpha_{\lambda,T} = \sum_{X,j} \alpha^{(X,j)}_{\lambda,T} + \alpha_{RI} + \alpha_{IB} \tag{13}$$

where the sum is extended to all X-species participating to the emitting medium and to all j-bound transitions denoted $k \to i$. The indices RI and IB refer to radiative ionization and inverse Bremsstrahlung, respectively. Under the gate delay conditions t where the experiments were performed, the electron density n_e is of the order of 10^{22} m^{-3}. The contribution to the spectrum of radiative ionization and inverse Bremsstrahlung is therefore negligible [77,78]. The absorption coefficient thus results from the contribution of each bound transition j due to the species X written as, including stimulated emission [79]

$$\alpha^{(X,j)}_{\lambda,T} = \frac{e^2}{4\epsilon_0 m_e c^2}\,\lambda^2\, f_{ik}\,\left[X_i\right]\,P(\lambda)\left(1 - e^{-\frac{hc}{\lambda k_B T_e}}\right) \tag{14}$$

where e is the electron charge, ϵ_0 the vacuum electric permittivity, m_e the electron mass, c the speed of light, f_{ik} the absorption oscillator strength of the transition, h the Planck's constant and k_B the Boltzmann's constant. $P(\lambda)$ is the normalized profile of the line emitted due to the Stark and Doppler effects [80]. The Stark effect is taken into account by the half width at half maximum of the line relative to the $k \to i$ transition concerned. This broadening is proportional to the electron density in a first approximation. Over the [653, 659] nm range, only the H_α line is well known concerning the relationship between the Stark broadening parameters and the electron density. Recently, a thorough experimental study has been reported by Mijatovic et al. [81] concerning the determination of $\Delta\lambda_{\alpha,S}$. In the following, we have therefore preferred to use these results rather than those reported by Gigosos et al. The D_α line has Stark broadening parameters very close to those of the hydrogen atom [82]. In the absence of reference data for tritium, we have assumed that isotopic effects remain negligible. Thus, the Stark broadening parameters of the T_α line are assumed to be identical to those of the H_α line. For the other lines, the default broadening recommended by Zeng et al. [83] is used. For Ti I lines in the [460, 475] nm spectral range, Hanif et al. [84] report a half width at half maximum of the order of 0.2 nm for an electron density of the order of 10^{22} m^{-3}. The Ti II lines seem to be characterized by an identical broadening. This value is consistent with the default value recommended by Zeng et al.. The results reported by Lednev et al. [85] over the [345, 400] nm range where a large number of Ti II lines are involved confirm that the Stark broadenings of the Ti I and Ti II lines are identical under low electron density conditions and are correctly reproduced by the Zeng et al. correlation. The Doppler broadening $\Delta\lambda_{ki,D}$ is proportional to $\sqrt{T_X/m_X}$ with T_X the kinetic temperature of the X species concerned of mass m_X. Here, equilibrium induces the equality $T_X = T_e$. An apparatus function is also taken into account. It is of the Lorentzian type for which width at half maximum depends on the diameter d_s of the optical fibers used to guide the light to the spectrometer and the spectral dispersion on the photodetector. Finally, $[X_i]$ is the population density of the lower level of the transition j considered for the species X.

Since the plasma is assumed to be at LTE, the values of $[X_i]$, and thus the composition of the plasma, can be calculated from the thermodynamic conditions if they are known. Since the gate delay $t = 10$ µs is large, the plasma is assumed to be relaxed in terms of expansion [86]. We therefore assume that its pressure is that of ambient argon, i.e. $p = 10^5$ Pa. Diffusion took place and argon is uniform within the plasma. It is also composed of other species depending on the nature of the sample on which the laser shots are performed.

3.6.1. Ti-Al-V sample

The complete characterisation of the plasma emitting the Ti-Al-V (TA6V sample) spectrum of Fig. 7 requires the determination of x_{Ar}, T_e and z_p.

1. x_{Ar}
   The atomic masses of Ti, Al and V are mutually quite close. Moreover, the diameter d_L of the laser spot is large compared to the characteristic grain size of the sample. Therefore, matrix effects can be expected to play a small role in the generation of the laser-induced plasma. Therefore, we assumed that the relative mole fractions of titanium, aluminium and vanadium in the plasma are the same as those in the TA6V sample. Argon is the main species due to the expansion of the plasma and to the late observation times favourable to the relaxation of the gradients by diffusion [87]. The mole fraction x_{Ar} of argon in the plasma is therefore close to unity.
2. T_e
   The spectrum of Fig. 7 for the TA6V sample shows several Ti^+ lines whose intensity ratio to Ti lines is very sensitive to temperature. To recover the experimental ratio, the temperature T_e cannot exceed 9000 K.
3. z_p
   For laser-induced plasmas obtained on a Si-O or Al-O alloy under nitrogen at atmospheric pressure at a fluence of the order of 80 J cm^{-2}, the plasma length is of the order of 700 µm at $t = 5$ µs [87]. For Si-O-Ba samples irradiated under argon at pressure $p = 5 \times 10^4$ Pa with a fluence of 100 J cm^{-2}, the plasma length is of the order of 850 µm at $t = 7$ µs [75]. The expansion dynamics over long times therefore remain rather slow. Argon is known to confine the plasma during its expansion. This action is all the more effective the higher the pressure. On the other hand, the higher the fluence, the more intense the initial expansion. In our conditions where argon is used as the ambient gas at a pressure of $p = 10^5$ Pa and the fluence is 260 J cm^{-2}, the length of the plasma can be considered to be of the order of 1000 µm at the gate delay $t = 10$ µs of observation.

We have determined by iteration the parameters x_{Ar}, T_e and z_p with the following constraints.

- Constraint on n_e
  The line broadenings (mostly due to the Stark effect) are identical to those obtained on the spectra of Pd-Ti/T-Si samples, where the presence of hydrogen and the knowledge of $\Delta\lambda_{\alpha,S}$ allow to estimate n_e with precision. The electron density is therefore of the order of 10^{22} m^{-3}.
- Constraints on the intensity of the Ti I lines at 655.483 and 655.606 nm
  The correlation proposed by Zeng et al. [83] tends to minimise the line broadenings. The Ti I lines at 655.483 and 655.606 nm have

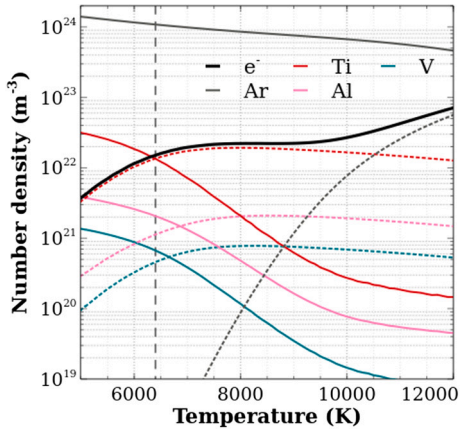

Fig. 11. Evolution with the temperature of the number density of atoms (thin continuous lines), ions (dashed lines) and electrons (thick black line) of a plasma at $p = 10^5$ Pa containing $x_{Ar} = 0.972$, $x_{Ti} = 2.41 \times 10^{-2}$, $x_{Al} = 2.86 \times 10^{-3}$, $x_V = 1.01 \times 10^{-3}$. With this composition, the Ti, Al and V relative mole fractions are the same as for the TA6V sample (cf. Table 4). The vertical dashed line is related to the value of T_e required to match the experimental spectrum (cf. Fig. 12).

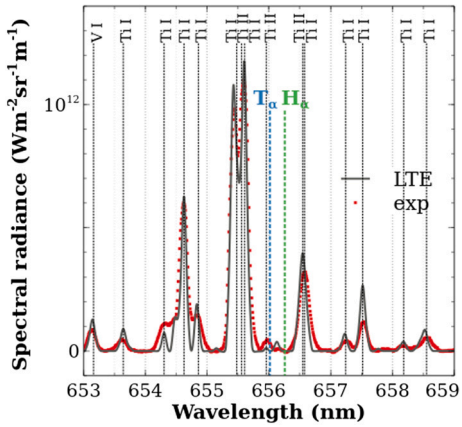

Fig. 12. Comparison between the experimental (exp) and the calculated (LTE) spectra with $x_{Ar} = 0.972$, $x_{Ti} = 2.41 \times 10^{-2}$, $x_{Al} = 2.86 \times 10^{-3}$, $x_V = 1.01 \times 10^{-3}$, $T_e = 6400$ K, $p = 10^5$ Pa and $z_p = 1300$ µm.

their Einstein coefficient referenced in the NIST database with an accuracy of 18% [21]. The iterative calculation is therefore performed by keeping a tolerance of the same order on the intensity of these lines and not on their maximum spectral radiance.

The final composition obtained after these iterative calculations is $x_{Ar} = 0.972$, $x_{Ti} = 2.41 \times 10^{-2}$, $x_{Al} = 2.86 \times 10^{-3}$, $x_V = 1.01 \times 10^{-3}$. Fig. 11 illustrates the evolution with temperature of the density of the species present. We can see that there is a plateau of electron density of 2×10^{22} m^{-3} around 8000 K. Around this temperature, the densities of Ti^+, Al^+ and V^+ remain constant while those of Ti, Al and V decrease with increasing temperature. This indicates an increase in the degree of ionization of the plasma. It should be noted that the [Al]/[Ti] and [V]/[Ti] ratios remain constant, as the [Al^+]/[Ti^+] and [V^+]/[Ti^+] ratios. They directly depend on the composition. They confirm that this composition is the same as the one of the sample.

If we consider a temperature $T_e = 6400$ K and a plasma length $z_p = 1300$ µm, the spectrum calculated over the interval [653, 659] nm is very close to the experimental spectrum obtained on the TA6V sample, as illustrated by Fig. 12. For the comparison displayed on Fig. 12, the background signal has been subtracted from the spectrum of Fig. 7. The vanadium line at 653.142 nm is indeed very well found (cf. Table 5). Its intensity is in the ratio of that of the titanium lines due to the assumption that the composition of titanium, aluminium and vanadium in the plasma is the same as in the sample. It is observed that the default Stark broadening does indeed tend to somewhat underestimate the experimental values. It is interesting to note that the Ti II lines are well reproduced. These lines have a high temperature sensitivity. Indeed, although the total density of Ti^+ (which is the main ion) is almost constant around 8000 K, a variation in temperature leads to a variation in the population density of the upper states of the Ti II transitions at 655.564, 655.959 and 656.550 nm. This then changes the intensity of these lines, moving the reconstructed spectrum away from the experimental spectrum. The temperature $T_e = 6400$ K is thus obtained. It leads to the value of the electron density $n_e = 1.6 \times 10^{22}$ m^{-3}. At this point, we do not develop an estimate of the uncertainty of the plasma parameters. This uncertainty is treated in section 3.6.3 for the tritiated sample.

The temperature obtained is fully consistent with that measured at long times under similar conditions [61,84,88,89]. In particular, the work reported by Khalil et al. [90] must be mentioned. They were carried out on pure Ti in air at atmospheric pressure using laser pulses of 8 ns duration at 532 nm under a laser irradiance of 1.35×10^{14} W m^{-2}. The temperature at $t = 6$ µs is in the range [4000, 7000] K. Except for the ambient gas and the composition of the sample, the conditions of Khalil et al. are very close to our own. As argon confines the plasma, the temperature is slightly higher than under air [91,92]. Studies have been devoted to a comparison of the temperature obtained around $t = 10$ µs on metal plasmas under similar irradiance conditions in argon and air (Aguilera et al. [93] on Fe, Gomes et al. [94] on Al-Cu, Aguilera & Aragon [95] on steel alloy). These studies have shown that the temperature obtained under argon is about 1000 K higher than that observed under air. Assuming that the same is true for the Ti-Al-V alloy, the range given by Khalil et al. can therefore be extended to [5000, 8000] K. The temperature $T_e = 6400$ K belongs to this range. It can be noted that the temperature values obtained under argon around $t = 10$ µs on these metallic materials are very close to the value of T_e determined here.

Aguilera et al. [96] report spectroscopic measurements made on a plasma obtained on a Fe-Ni alloy in air at atmospheric pressure under an irradiance similar to our experiments, but at the wavelength 1064 nm. They obtain a plasma radius measured parallel to the surface of 2000 µm around $t = 15$ µs. This value is quite close to the $z_p = 1300$ µm value obtained in our case at $t = 10$ µs. The same authors give after Abel inversion a mapping of the electron density and temperature in the case of Fe irradiated under the same conditions in air and argon. It should be noted that the uniformity of the plasma is observed under argon. Around $t = 9 - 11$ µs, the plasma obtained under air has a larger diameter than under argon, with an equivalent z_p length. This indicates that the aerodynamic behaviour of the plasma depends strongly on the nature of the external gas. Under argon, the length of the zone with the highest values of electron density and temperature is about 1200-1400 µm. These are the most emissive zones, and therefore the ones responsible for the observed spectrum. The $z_p = 1300$ µm value determined here belongs to this interval.

On Fe in argon at 1064 nm, the value of the electron density measured by Aguilera et al. [93] is of the order of 2×10^{22} m^{-3} around $t = 9 - 11$ µs. This is very close to our result. For Fe-Ni alloy in air at 1064 nm, the value of the electron density measured by Aguilera et al. [96] is of the order of 7×10^{21} m^{-3} around $t = 15 - 18$ µs. For Aguilera & Aragon [95] at 1064 nm on steel under argon, the electron density is 2.6×10^{22} m^{-3} at $t = 12$ µs. On Ti, Hanif et al. [84] report an electron density between 5×10^{21} m^{-3} and 1.5×10^{22} m^{-3} in air at 532 nm under similar irradiance conditions to ours around $t = 3.5$ µs. For a higher gate delay, the electron density will have decreased and under argon, it will have increased. Given the low dynamics at long times, it can be expected that for Ti the electron density values will not have funda-

Table 8
Estimation of the X atoms number in the gas phase from the ablation and from the calculation of the spectrum in Fig. 14.

Element X	Pd	Ti	H-T	Si	All
N_X from ablation	1.4×10^{13}	3.0×10^{13}	2.5×10^{14}	1.8×10^{14}	4.7×10^{14}
N_X from the spectra	1.1×10^{12}	6.6×10^{12}	2.0×10^{14}	8.3×10^{13}	2.9×10^{14}

mentally changed. The value obtained here of $n_e = 1.6\times10^{22}$ m^{-3} is therefore quite consistent with these results.

This section has therefore shown that the reconstruction of the spectrum obtained under our observational conditions is possible assuming LTE and uniformity of the plasma produced. Moreover, the procedure adopted to reconstruct this spectrum leads to the composition, the density and the electron temperature values in coherence with direct experimental results. This procedure has therefore been reproduced for the Pd-Ti/T-Si sample.

3.6.2. Pd-Ti/T-Si sample

The spectra in Fig. 9 show a rapid collapse in the intensity of the titanium lines from one shot to another. We have shown in the previous section the crucial role played by these lines in the reconstruction of the spectrum. In the following, we have therefore only focused on shot 1. As previously, the procedure is governed by certain constraints.

- Constraint on n_e
  The broadenings of the Ti lines in the spectra of Fig. 7 are identical. The value $n_e = 1.6\times10^{22}$ m^{-3} of the electron density determined previously is therefore retained.
- Constraint on p
  Since the observation times $t = 10$ µs are the same, the thermodynamic conditions discussed previously remain valid. Thus, the plasma pressure is $p = 10^5$ Pa.
- Constraint on T_e
  The Ti II lines keep their strong dynamics. The temperature T_e cannot exceed 9000 K. Moreover, the pressure being the same as in the Ti-Al-V case, the product between the total density $\sum_i[X_i]$ and the temperature is conserved. Since the electron density is also conserved as is the total ion density by electroneutrality, the only way to obtain a lower Ti I line intensity than in the Ti-Al-V case is to have a lower neutral density and therefore a higher plasma temperature.
- Constraint on x_{Ti}/x_{Pd} ratio
  The Pd and Ti layers of the Pd-Ti/T-Si sample absorb the laser radiation. We have assumed that the ratio x_{Ti}/x_{Pd} in the plasma is equal to the ratio of the thicknesses of the layers involved.
- Constraint on z_p
  The discussion of z_p in the previous section showed that its value is rather weakly dependent on the nature of the sample. This value further depends on the nature of the ambient gas. We have therefore retained the value $z_p = 1300$ µm determined for the Ti-Al-V sample.

With mole fractions $x_{Ar} = 0.922$, $x_{Pd} = 4.62\times10^{-4}$, $x_{Ti} = 1.76\times10^{-3}$, $x_{Si} = 2.2\times10^{-2}$, $x_H = 2.74\times10^{-2}$ and $x_T = 2.68\times10^{-2}$, Fig. 13 shows the evolution of the plasma composition with temperature at $p = 10^5$ Pa. It can be seen that the electron density is close to 10^{22} m^{-3} around 8000 K. The best agreement with the experimental spectrum is shown on Fig. 14 where the temperature is 8900 K. In these conditions, the calculated spectrum radiance differs from the experimental one by 3% (see section 3.6.3).

One can compare the temperature levels obtained in the two situations where the sample is or is not charged with H-T. For simplicity, we can consider that the plasma is metallic and that its average density $\bar{\rho}$ during the absorption phase of the laser pulse is insensitive to the presence of hydrogen isotopes because of their very low atomic mass. By

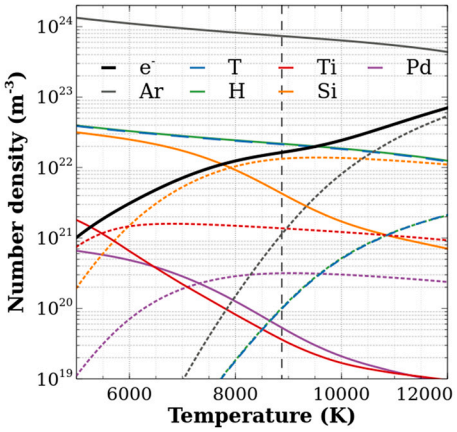

Fig. 13. Evolution with the temperature of the number density of atoms (thin continuous lines), ions (dashed lines) and electrons (thick black line) of a plasma at $p = 10^5$ Pa containing $x_{Ar} = 0.922$, $x_{Pd} = 4.62\times10^{-4}$, $x_{Ti} = 1.76\times10^{-3}$, $x_{Si} = 2.2\times10^{-2}$, $x_H = 2.74\times10^{-2}$ and $x_T = 2.68\times10^{-2}$. The vertical dashed line is related to the value of T_e required to match the experimental spectrum (cf. Fig. 14). H and T overlap.

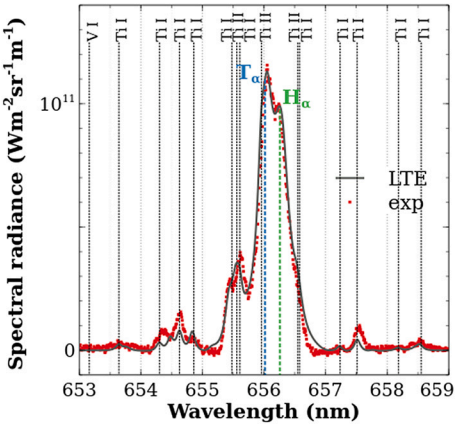

Fig. 14. Comparison between the experimental (exp) and the calculated (LTE) spectra with $x_{Ar} = 0.922$, $x_{Pd} = 4.62\times10^{-4}$, $x_{Ti} = 1.76\times10^{-3}$, $x_{Si} = 2.2\times10^{-2}$, $x_H = 2.74\times10^{-2}$, $x_T = 2.68\times10^{-2}$, $T_e = 8900$ K, $p = 10^5$ Pa and $z_p = 1300$ µm.

conservation of energy, the plasma specific enthalpy immediately after absorption of the laser pulse is

$$h(\tau_L, x_{H-T}) = h(0, x_{H-T}) + \frac{\alpha_L(x_{H-T})}{z_{Si}(x_{H-T})}\frac{F_L}{\bar{\rho}} \tag{15}$$

in which $h(0, x_{H-T})$ is its initial specific enthalpy and $\alpha_L(x_{H-T})$ is the spectral absorptivity of the sample. The presence of hydrogen isotopes leads to a reduction in the absorption of the sample (see section 3.2). It also plays an important role concerning z_{Si} by virtue of (5) through the thermal diffusivity a_{Si} dependence. Owing to the link between a_{Si}, the density $\rho(0)$, the specific heat $c_{Si}(x_{H-T})$ and the thermal conductivity $k_{Si}(x_{H-T})$ of the ablated material, we deduce

$$h(\tau_L, x_{H-T}) = h(0, x_{H-T}) + \frac{F_L}{\bar{\rho}}\sqrt{\frac{\rho(0)}{\tau_L}}\,\alpha_L(x_{H-T})\sqrt{\frac{c_{Si}(x_{H-T})}{k_{Si}(x_{H-T})}} \tag{16}$$

The influence of the presence of hydrogen isotopes on the specific enthalpy obtained after absorption of the pulse is therefore in the factor

$$\gamma(x_{H-T}) = \alpha_L(x_{H-T}) \sqrt{\frac{c_{Si}(x_{H-T})}{k_{Si}(x_{H-T})}} \tag{17}$$

Even if α_L decreases when x_{H-T} increases, c_{Si} increases very strongly when x_{H-T} increases. Roura et al. [97] have indeed shown that c_{Si} increases by 10% when x_H increases by 2%. Coupled with the fact that k_{Si} decreases when x_H increases [98] and assuming a similar behaviour for tritium, we deduce that γ increases when x_{H-T} increases. The specific enthalpy variation $h(\tau_L, x_{H-T}) - h(0, x_{H-T})$ is then higher in the presence of hydrogen isotopes. Since the plasma is essentially argon, its temperature is likely to be higher in the presence of hydrogen isotopes. The results obtained above are therefore consistent with the analysis developed here.

Finally, the conservation of the number of atoms can be verified. First, the number of plasma constituents can be estimated by the ablation discussed in section 3.2. It is assumed that the laser-matter interaction leads to the solid→gas transition of a cylindrical cone of diameter d_L and height z_{Si}, limited by two successive layers of Pd and Ti of thickness z_{Pd} and z_{Ti}, respectively. Assuming a charge of 0.7 H-T atoms for a palladium atom, 2 H-T atoms for a titanium atom and 1 H-T atom for a silicon atom (see section 2.2), we obtain the numbers of atoms ending up in the gas phase listed in Table 8. The number of atoms in the gas phase can also be estimated by the mole fractions to recover the spectrum in Fig. 14. The total density in the plasma of pressure p and temperature T_e is $p/(k_B T_e)$. The density of ions and neutrals is therefore $p/(k_B T_e) - n_e$. The density of heavies other than argon is consequently $(1 - x_{Ar})\left[p/(k_B T_e) - n_e\right]$. The plasma is assumed to be bounded by a half-sphere of radius z_p resting on the sample. The mole fraction of the species X being x_X, the number of atoms involved in the plasma is

$$N_X = x_X \frac{2}{3}\pi z_p^3 \left(1 - x_{Ar}\right) \left(\frac{p}{k_B T_e} - n_e\right) \tag{18}$$

Table 8 gives the values. The results depart from a factor of 2 to 10. Let us remind that very simple assumptions have been made to estimate N_X in both cases. Nevertheless, this opens the question of the uncertainty of the previous composition determination.

3.6.3. Uncertainty estimate

We have defined the relative deviation from the radiance experimentally observed on the $[\lambda_1, \lambda_2]$ spectral range by

$$\Delta_{\lambda_1}^{\lambda_2} = \frac{\int_{\lambda_1}^{\lambda_2} L_\lambda \, d\lambda - \int_{\lambda_1}^{\lambda_2} L_\lambda^{exp} \, d\lambda}{\int_{\lambda_1}^{\lambda_2} L_\lambda^{exp} \, d\lambda} \tag{19}$$

where L_λ^{exp} is the experimental spectral radiance without the background contribution. The relative deviation $\Delta_{\lambda_1}^{\lambda_2}$ leads to quantify the uncertainty in the agreement with the experimental spectrum, the uncertainty of the conversion in spectral radiance being disregarded.

An optimization procedure is implemented to search the values of the parameters n_e, T_e, z_p, x_{Si}, x_H/x_T and x_T/x_{Ti} minimizing $\Delta_{\lambda_1}^{\lambda_2}$ on the [654, 658] nm spectral range. The ratios x_H/x_T and x_T/x_{Ti} are considered since they have a direct influence of the relative contribution of the H, T and Ti lines in the spectrum on this spectral range. The plasma characteristics of section 3.6.2 correspond to a minimum for $\Delta_{\lambda_1}^{\lambda_2}$ of 3%. To illustrate the uncertainty of the determination, Table 9 gives the values of $\Delta_{\lambda_1}^{\lambda_2}$ on the [654, 658] nm spectral range for different values of each parameter, all the others keeping the value derived from the minimization procedure. If we consider that the uncertainty on the spectrum reconstruction on the [654, 658] nm spectral range is $\Delta_{\lambda_1}^{\lambda_2} = 3\%$, one deduces the uncertainty on the determination of each parameter as the difference between its final value and the value required to obtain $\Delta_{\lambda_1}^{\lambda_2} = 0$.

For instance, the n_e value leading to $\Delta_{\lambda_1}^{\lambda_2} = 0$ derived from Table 9 is 1.61×10^{22} m^{-3}. The final value is 1.65×10^{22} m^{-3}. The absolute uncertainty is then 4×10^{20} m^{-3}, in other words the relative uncertainty is $\sim$ 2%, i.e. $\pm$ 1%. Since electron density drives the Stark broadening, the uncertainty in terms of wavelength calibration has to be included. Moreover, the assumptions made about the Stark broadening parameters have to be considered, but their impact is difficult to evaluate. All these contributions should be added to the $\sim$ 2% estimated above. We do not further develop this aspect.

For T_e, the previous procedure leads to 40 K of uncertainty. Let us remind that the T_e value drives the population density of the upper level of the transitions, therefore the radiance of the lines, then their spectral radiance distribution owing to their broadening. Since the agreement with the experimental spectrum is estimated through the radiance, the previous uncertainty has to be added to the one due to the pyrometer. The latter uncertainty is close to 40 K ($\pm$ 20 K). Including the uncertainty on the tungsten ribbon lamp current setting, the total uncertainty is therefore $\sim$ 100 K ($\pm$ 50 K).

The uncertainty on z_p first estimated by Table 9 is $\sim$ 40 μm, therefore $\sim$ 3%. But at constant parameters, changing the z_p value leads to the linear modification of the radiance of the spectrum. Indeed, the transitions over the [654, 658] nm spectral range are optically thin. The uncertainty resulting from the calibration procedure has to be added. As a result, the final uncertainty on the determination of z_p is $\sim$ 19% ($\sim \pm$ 10%).

The uncertainty on x_{Si} is significant. Assuming linearity of the evolution of $\Delta_{\lambda_1}^{\lambda_2}$ with x_{Si}, the value $x_{Si} = 1.38 \times 10^{-2}$ is necessary to have $\Delta_{\lambda_1}^{\lambda_2} = 0$. The relative uncertainty is therefore $(2.2 \times 10^{-2} - 1.38 \times 10^{-2})/2.2 \times 10^{-2} = 37\%$. This important value can be explained by the role played by silicon. Indeed, as illustrated by Fig. 13, Si acts as an ions provider allowing to reach by electroneutrality a sufficiently high electron density close to that experimentally observed. This means that if Si is not included in the composition, it is impossible to reproduce the experimental spectrum. The silicon mole fraction uncertainty is therefore a function of the uncertainty of n_e and T_e through the Saha equilibrium law. Anyway, the uncertainty has no particular influence in the present case.

Working on x_H/x_T is more interesting because this ratio directly drives the spectrum in terms of relative hydrogen/tritium contribution and is therefore completely independent of the uncertainty of the spectral radiance calibration. With the same procedure as the one used above to estimate the electron density uncertainty, we obtain an absolute uncertainty of 0.01 for this ratio, therefore a relative uncertainty of 9% ($\sim \pm$ 5%). This uncertainty includes the perturbation of the titanium lines since it is based on the radiance on the [654, 658] nm spectral range and the noise of the signals. The spectral radiance calibration playing no role, we can conclude that this value of 9% is the final relative uncertainty on the hydrogen/tritium ratio inside the ablated material. Similar conclusions can be derived regarding the x_T/x_{Ti} ratio. Table 9 leads to a 5% uncertainty on its value.

4. Conclusion

The detection of tritium by LIBS in a metallic material is reported. The material concerned is a silicon substrate on which a 55 nm thick layer of titanium and an external 16 nm thick layer of palladium have been deposited by sputtering. The material is loaded by infusion first with hydrogen for 1 hour, then with tritium for 64 hours at 573 K under a pressure slightly higher than 10^5 Pa. The tritium concentration thus obtained is close to saturation in the thin films and significant over the first hundred nanometers in the silicon substrate.

Using a specifically designed device equipped with a top-hat type laser source, we irradiated the sample with an energy of 25 mJ for 6.9 ns on a spot of 110 μm in diameter. The sample was placed in argon at atmospheric pressure.

Table 9
Values of $\Delta_{\lambda_1}^{\lambda_2}$ (defined by equation (19)) on the [654, 658] nm spectral range for different values of n_e, T_e, z_p, x_{Si}, x_H/x_T and x_T/x_{Ti}. When a parameter is modified, the value of the other parameters remains unchanged with respect to the final value.

Parameter (unit)	Value	$\Delta_{\lambda_1}^{\lambda_2}$ (%)	Parameter (unit)	Value	$\Delta_{\lambda_1}^{\lambda_2}$ (%)
	1.25×10^{22}	-29.3		8675	-9.3
	1.45×10^{22}	-13.3		8775	-4.0
n_e (m^{-3})	1.65×10^{22}	3.1	T_e (K)	8875	3.1
	1.85×10^{22}	20.8		8975	11.8
	2.05×10^{22}	39.4		9075	21.5
	1100	-12.7		1.8×10^{-2}	1.4
	1200	-4.8		2.0×10^{-2}	2.4
z_p (μm)	1300	3.1	x_{Si}	2.2×10^{-2}	3.1
	1400	11.1		2.4×10^{-2}	3.8
	1500	19.0		2.6×10^{-2}	4.4
	0.82	-4.0		13.25	-6.4
	0.92	-0.2		14.25	-1.1
x_H/x_T	1.02	3.1	x_T/x_{Ti}	15.25	3.1
	1.12	6.8		16.25	8.1
	1.22	10.5		17.25	13.0

The laser-induced plasma spectrum has been analyzed in detail over the [653,659] nm spectral range centered on the α lines of the Balmer series. This spectrum includes titanium, hydrogen and tritium lines. By comparison with that obtained on an uncharged sample, this spectrum highlighted the modification of the properties of the material induced by the infusion process. Shots performed at the same location revealed the increased diffusion of hydrogen compared to tritium within the material. The observation times, quite late, allow a sufficient reduction in the electron density of the laser-induced plasma leading to sufficient spectral resolution and to the distinct observation of the lines of hydrogen and tritium despite a significant overlapping.

The presence of argon and the chosen observation times allow the plasma to be in the conditions of local thermodynamic equilibrium at known pressure. Argon on the other hand ensures that it is uniform. The plasma spectrum can therefore be calculated from the solution of the radiative transfer equation. We checked the validity of this calculation by retrieving precisely the spectrum obtained experimentally on a Ti-Al-V sample for which the composition is known. The procedure thus verified, we reproduced it for the sample containing tritium and hydrogen. Its composition was then deduced. We obtained a composition satisfactorily compatible with the conditions of preparation of the sample.

This possibility of detecting tritium by LIBS will be applied to tritiated bulk tungsten samples to go further in verifying its applicability to the PFCs characterization.

CRediT authorship contribution statement

Aurélien Favre: investigation, writing. **Arnaud Bultel:** conceptualization, supervision, writing. **Mickael Payet:** tritiation, deuteration of the samples. **Stéphane Vartanian:** experiments on tritiated samples. **Sébastien Garcia-Argote:** safety of the experiments on tritiated samples. **Vincent Morel:** supervision. **Elodie Bernard:** experimental resources. **Sabina Markelj:** characterization of the samples. **Miha Čekada:** preparation of the samples. **Etienne Hodille:** analysis. **Alexnadre Semerok:** analysis. **Christian Grisolia:** resources, project management.

Declaration of competing interest

The authors declare that they have no known competing financial interests or personal relationships that could have appeared to influence the work reported in this paper.

Data availability

Data will be made available on request.

Acknowledgements

We thank the TRANSAT project funded by the Euratom Research and Training Programme 2014-2018 under grant agreement No 754586. This work has been carried out within the framework of the French Federation for Magnetic Fusion Studies (FR-FCM) and of the Eurofusion consortium, and has received funding from the Euratom Research and Training Programme 2014-2018 and 2019-2023 under grant agreement No 633053. The views and opinions expressed herein do not necessarily reflect those of the European Commission. We also thank the *Agence Nationale de la Recherche* (ANR), through the program "*Investissement d'Avenir*" (ANR-10-LABX-09-01), LabEx EMC 3, PICOLIBS project and through the program "*Investissement d'Avenir*" (ANR-10-LABX-09-01), LabEx EMC 3, PTOLEMEE project. This work has been also partially financed by the "Region Normandie", France and the European Regional Development Fund (ERDF) of the European Union, ZEOMETHYL project. The views by Scanning Electron Microscope have been obtained by Fabien Cuvilly from the GPM laboratory, UMR 6634, CNRS, University and INSA Rouen-Normandie.

References

[1] R. Parker, G. Janeschitz, H.D. Pacher, D. Post, S. Chiocchio, G. Federici, P. Ladd, ITER Joint Central Team, Home Teams, Plasma-wall interactions in ITER, J. Nucl. Mater. 241–243 (1997) 1–26, https://doi.org/10.1016/S0022-3115(97)80027-X.
[2] E.A. Hodille, E. Bernard, S. Markelj, J. Mougenot, C.S. Becquart, R. Bisson, C. Grisolia, Estimation of the tritium retention in ITER tungsten divertor target using macroscopic rate equations simulations, Phys. Scr. T 170 (2017) 014033, https://doi.org/10.1088/1402-4896/aa8787.
[3] J. Roth, E. Tsitrone, T. Loarer, V. Philipps, S. Brezinsek, A. Loarte, G.F. Counsell, R.P. Doerner, K. Schmid, O.V. Ogorodnikova, R.A. Causey, Tritium inventory in ITER plasma-facing materials and tritium removal procedures, Plasma Phys. Control. Fusion 50 (2008) 103001, https://doi.org/10.1088/0741-3335/50/10/103001.
[4] M. Klimenkov, P. Vladimirov, J. Hoffmann, N. Zimber, A. Moslang, V. Kuksenko, First simultaneous detection of helium and tritium inside bubbles in beryllium, Micron 127 (2019) 102754, https://doi.org/10.1016/j.micron.2019.102754.
[5] M. Prem, G. Krexner, J. Pleschiutschnig, Helium damage in long-aged metal-tritium systems, J. Alloys Compd. 356–357 (2003) 683–687, https://doi.org/10.1016/S0925-8388(02)01290-2.
[6] S. Yang, J.-U. Lee, H.-G. Kang, M.H. Chang, T. Oda, Tritium and helium embrittlement of austenitic steels used in tritium storage and delivery systems, J. Nucl. Mater. 540 (2020) 152349, https://doi.org/10.1016/j.jnucmat.2020.152349.
[7] G. Counsell, P. Coad, C. Grisolia, C. Hopf, W. Jacob, A. Kirschner, A. Kreter, K. Krieger, J. Likonen, V. Philipps, J. Roth, M. Rubel, E. Salancon, A. Semerok, F.L. Tabares, A. Widdowson, JET EFDA contributors, Tritium retention in next step devices and the requirements for mitigation and removal techniques, Plasma Phys.

Control. Fusion 48 (2006) B189–B199, https://doi.org/10.1088/0741-3335/48/12B/S18.
[8] A. Widdowson, A. Baron-Wiechec, P. Batistoni, E. Belonohy, J.P. Coad, P. Dinca, D. Flammini, F. Fox, K. Heinola, I. Jepu, J. Likonen, S. Lilley, C.P. Lungu, G.F. Matthews, J. Naish, O. Pompilian, C. Poroniscu, M. Rubel, R. Villari, JET contributors, Experience of handling beryllium, tritium and activated components from JET ITER like wall, Phys. Scr. T 167 (2016) 014057, https://doi.org/10.1088/0031-8949/T167/1/014057.
[9] F. Le Guern, F. Brygo, P. Fichet, E. Gauthier, C. Hubert, C. Lascoutuna, D. Menut, S. Mousset, A. Semerok, M. Tabarant, J.M. Weulersse, Co-deposited layer characterization and removal control by optical emission spectroscopy coupled to nano-second laser ablation, Fusion Eng. Des. 81 (2006) 1503–1509, https://doi.org/10.1016/j.fusengdes.2005.09.081.
[10] A.W. Miziolek, V. Palleschi, I. Schechter, Laser-Induced Breakdown Spectroscopy (LIBS) Fundamentals and Applications, Cambridge University Press, 2006.
[11] R. Noll, C. Fricke-Begemann, S. Connemann, C. Meinhardt, V. Sturm, LIBS analyses for industrial applications - an overview of developments from 2014 to 2018, J. Anal. At. Spectrom. 33 (2018) 945, https://doi.org/10.1039/c8ja00076jrsc.li/jaas.
[12] M.A. Khater, Trace detection of light elements by laser-induced breakdown spectroscopy (LIBS): applications to NonConducting materials, Opt. Spectrosc. 115 (2013) 574–590, https://doi.org/10.1134/S0030400X13100123.
[13] W.T.Y. Mohamed, Improved LIBS limit of detection of Be, Mg, Si, Mn, Fe and Cu in aluminum alloy samples using a portable Echelle spectrometer with ICCD camera, Opt. Laser Technol. 40 (2008) 30–38, https://doi.org/10.1016/j.optlastec.2007.04.004.
[14] J. Hermann, E. Axente, F. Pelascini, V. Craciun, Analysis of multi-elemental thin films via calibration-free Laser-Induced Breakdown Spectroscopy, Anal. Chem. 91 (2019) 2544–2550, https://doi.org/10.1021/acs.analchem.8b05780.
[15] H.J. van der Meiden, S. Almaviva, J. Butikova, V. Dwivedi, P. Gasior, W. Gromelski, A. Hakola, X. Jiang, I. Jogi, J. Karhunen, M. Kubkowska, M. Laan, G. Maddaluno, A. Marín-Roldan, P. Paris, K. Piip, M. Pisarcik, G. Sergienko, M. Veis, P. Veis, S. Brezinsek EUROfusion WP PFC Team, Monitoring of tritium and impurities in the first wall of fusion devices using a LIBS based diagnostic, Nucl. Fusion 61 (2021) 125001, https://doi.org/10.1088/1741-4326/ac31d6.
[16] A. Favre, M. Lesage, V. Morel, A. Bultel, P. Boubert, MERLIN, a RT-LTE software supporting the diagnostic application of LIBS to h-isotopes measurements, in: Proc. International Workshop on Laser-Induced Breakdown Spectroscopy, University of Szeged, Dec 2020, Szeged, Hungary, 2020.
[17] A. Bultel, V. Morel, A. Favre, G. Godard, A. Benyagoub, I. Monnet, A. Semerok, M. Dinescu, S. Markelj, P. Magaud, C. Grisolia, Towards ps-LIBS tritium measurements in W/Al materials, Fusion Eng. Des. 146 (2019) 1971–1974, https://doi.org/10.1016/j.fusengdes.2019.03.079.
[18] B.C. Windom, D.W. Hahn, Laser ablation—laser induced breakdown spectroscopy (LA-LIBS): a means for overcoming matrix effects leading to improved analyte response, J. Anal. At. Spectrom. 24 (2009) 1665–1675, https://doi.org/10.1039/b913495f.
[19] A.J. Effenberger, J.R. Scott, Effect af atmospheric conditions on LIBS spectra, Sensors 10 (2010) 4907–4925, https://doi.org/10.3390/s100504907.
[20] I. Jogi, J. Ristkok, J. Raud, J. Butikova, K. Mizohata, P. Paris, Laser induced breakdown spectroscopy for hydrogen detection in molybdenum at atmospheric pressure mixtures of argon and nitrogen, Fusion Eng. Des. 179 (2022) 113131, https://doi.org/10.1016/j.fusengdes.2022.113131.
[21] A. Kramida, Yu. Ralchenko, J. Reader, NIST ASD Team, NIST Atomic Spectra Database (ver. 5.9) [Online]. Available: https://physics.nist.gov/asd [2022, August], National Institute of Standards and Technology, Gaithersburg, MD, 2021.
[22] S.S. Srinivisan, P.C. Sharma, E.K. Stefanakos, D. Yogi Goswami, in: S.A. Sherif, D. Yogi Goswami, E.K. Stefanakos, A. Steinfeld (Eds.), Metal Hydrides Handbook of Hydrogen Energy, CRC Press, 2014, pp. 667–683.
[23] E. Wicke, H. Brodowsky, H. Zuchner, Hydrogen in palladium and palladium alloys, in: Hydrogen in Metals II, in: G. Alefeld, J. Volkl (Eds.), Topics in Applied Physics, vol. 29, Springer, Berlin, Heidelberg, 1978.
[24] D. Eliezer, T.H. Böllinghaus, Hydrogen effects in titanium alloys, in: R.P. Gangloff, B.P. Somerday (Eds.), Gaseous Hydrogen Embrittlement of Materials in Energy Technologies, in: Metals and Surface Engineering, Woodhead Publishing Series, vol. 1, 2012, pp. 668–706.
[25] L. Song, Z. Hu, D. Lin, D. Yang, X. Yu, Progress of hydrogenation engineering in crystalline silicon solar cells: a review, J. Phys. D, Appl. Phys. 55 (2022) 453002, https://doi.org/10.1088/1361-6463/ac9066.
[26] R.P. Santandrea, R.G. Behrens, A review of the thermodynamics and phase relationships in the palladium-hydrogen, palladium-deuterium and palladium-tritium systems, High Temp. Mater. Process. 7 (1986) 149–169, https://doi.org/10.1515/HTMP.1986.7.2-3.149.
[27] H.K. Birnbaum, C.A. Wert, Diffusion of hydrogen in metals, Ber. Bunsenges. Phys. Chem. 76 (1972) 806–816, https://doi.org/10.1002/bbpc.19720760835.
[28] Y. Lu, P. Zhang, First-principles study of temperature-dependent diffusion coefficients: hydrogen, deuterium and tritium in α-Ti, J. Appl. Phys. 113 (2013) 193502, https://doi.org/10.1063/1.4805362.
[29] T. Ichimiya, A. Furuichi, On the solubility and diffusion coefficient of tritium in single crystals of silicon, Int. J. Appl. Radiat. Isot. 19 (1968) 573–578, https://doi.org/10.1016/0020-708X(68)90067-7.
[30] S.J. Pearton, Hydrogen in crystalline silicon, Mater. Res. Soc. Symp. Proc. 59 (1985) 457–468, https://doi.org/10.1557/PROC-59-457.
[31] H. Buchold, G. Sicking, Proc. of Int. Meeting on H in Metals, Julich, Conf. 6 (II), 391, Cited in [27], 1972.
[32] G. Panzarini, L. Colombo, Hydrogen diffusion in silicon from tight-binding molecular dynamics, Phys. Rev. Lett. 73 (1994) 1636–1640, https://doi.org/10.1103/PhysRevLett.73.1636.
[33] N.M. Johnson, C. Herring, D.J. Chadi, Interstitial hydrogen and neutralization of shallow-donor impurities in single-crystal silicon, Phys. Rev. Lett. 56 (1986) 769–772, https://doi.org/10.1103/PhysRevLett.56.769.
[34] K. Oura, V.G. Lifshits, A.A. Saranin, A.V. Zotov, M. Katayama, Hydrogen interaction with clean and modified silicon surfaces, Surf. Sci. Rep. 35 (1999) 1–69, https://doi.org/10.1016/S0167-5729(99)00005-9.
[35] D. Mathiot, Modeling of hydrogen diffusion in n- and p-type silicon, Phys. Rev. B 40 (1989) 5867–5870, https://doi.org/10.1103/PhysRevB.40.5867.
[36] W.B. Jackson, C.C. Tsai, Hydrogen transport in amorphous silicon, Phys. Rev. B 45 (1992) 6564–6581, https://doi.org/10.1103/PhysRevB.45.6564.
[37] R. Rizk, P. de Mierry, D. Ballutaud, M. Aucouturier, D. Mathiot, Hydrogen diffusion and passivation processes in p- and n-type crystalline silicon, Phys. Rev. B 44 (1991) 6141–6151, https://doi.org/10.1103/PhysRevB.44.6141.
[38] N.M. Johnson, Mechanism for hydrogen compensation of shallow-acceptor impurities in singl-crystal silicon, Phys. Rev. B 31 (1985) 5525–5528, https://doi.org/10.1103/PhysRevB.31.5525.
[39] M. Capizzi, A. Mittiga, Hydrogen in crystalline silicon: a deep donor?, Appl. Phys. Lett. 50 (1987) 918–920, https://doi.org/10.1063/1.98032.
[40] N.H. Nickel, W.B. Jackson, J. Walker, Hydrogen migration in polycrystalline silicon, Phys. Rev. B 53 (1996) 7750–7761, https://doi.org/10.1103/PhysRevB.53.7750.
[41] B.L. Sopori, X. Deng, J.P. Benner, A. Rohatgi, P. Sana, S.K. Estreicher, Y.K. Park, M.A. Roberson, Hydrogen in silicon: a discussion of diffusion and passivation mechanisms, Sol. Energy Mater. Sol. Cells (1996) 159–169, https://doi.org/10.1016/0927-0248(95)00098-4.
[42] M. Stutzmann, W. Beyer, L. Tapfer, C.P. Herrero, States of hydrogen in crystalline silicon, Physica B 170 (1991) 240–244, https://doi.org/10.1016/0921-4526(91)90130-7.
[43] B. Liu, K.P. Chen, N.P. Kherani, T. Kosteski, K.R. Leong, S. Zukotynski, Self-irradiation enhanced tritium solubility in hydrogenated amorphous and crystalline silicon, J. Appl. Phys. 109 (2011) 054902, https://doi.org/10.1063/1.3549145.
[44] Y. Li, Y.T. Cheng, Hydrogen diffusion and solubility in palladium thin films, Int. J. Hydrog. Energy 21 (1996) 281–291, https://doi.org/10.1016/0360-3199(95)00094-1.
[45] T. Li, C. Zhou, Z. Liu, W. Wang, Computational and experimental study of nanosecond laser ablation of crystalline silicon, Int. Commun. Heat Mass Transf. 38 (2011) 1041–1043, https://doi.org/10.1016/j.icheatmasstransfer.2011.05.010.
[46] R.L. Kurucz, B. Bell, Atomic Line Data, Kurucz CD-ROM No. 23, Smithsonian Astrophysical Observatory, Cambridge, Mass, 1995.
[47] P.A.M. Van Hoof, Recent developments of the atomic line list, Galaxies 6 (2018) 63, https://doi.org/10.3390/galaxies6020063.
[48] W.L. Wiese, J.R. Fuhr, Accurate atomic transition probabilities for hydrogen, helium, and lithium, J. Phys. Chem. Ref. Data 38 (2009) 565–719, https://doi.org/10.1063/1.3077727.
[49] L. Torrisi, F. Caridi, L. Giuffrida, Comparison of Pd plasmas produced at 532 nm and 1064 nm by a Nd: YAG laser ablation, Nucl. Instrum. Methods Phys. Res. B 268 (2010) 2285–2291, https://doi.org/10.1016/j.nimb.2010.03.029.
[50] H. Reimers, J. Gold, B. Kasemo, D. Chakarov, Topographical and surface chemical characterization of nanosecond pulsed-laser micromachining of titanium at 532-nm wavelength, Appl. Phys. A 77 (2003) 491–498, https://doi.org/10.1007/s00339-002-1477-6.
[51] V. Schutz, U. Stute, A. Horn, Thermodynamic investigations on the laser ablation rate of silicon over five fluence decades, Phys. Proc. 41 (2013) 640–649, https://doi.org/10.1016/j.phpro.2013.03.128.
[52] A. Favre, V. Morel, A. Bultel, G. Godard, S. Idlahcen, M. Diez, C. Grisolia, F. Perry, Interface detection by picosecond Laser-Induced Breakdown Spectroscopy (LIBS): Application to a physical vapor deposited tungsten layer on a copper-chromium-zirconium substrate, Opt. Laser Technol. 150 (2022) 107913, https://doi.org/10.1016/j.optlastec.2022.107913.
[53] J.I. Avila, R.J. Matelon, R. Trabol, M. Favre, D. Lederman, U.G. Volkmann, A.L. Cabrera, Optical properties of Pd thin films exposed to hydrogen studied by transmittance and reflectance spectroscopy, J. Appl. Phys. 107 (2010) 023504, https://doi.org/10.1063/1.3272047.
[54] K.J. Palm, J.B. Murray, T.C. Narayan, J.N. Munday, Dynamic optical properties of metal hydrides, ACS Photonics 5 (2018) 4677–4686, https://doi.org/10.1021/acsphotonics.8b01243.
[55] K. Bucher, J. Bruns, H.G. Wagemann, Absorption coefficient of silicon: an assessment of measurements and the simulation of temperature variation, J. Appl. Phys. 75 (1994) 1127–1132, https://doi.org/10.1063/1.356496.
[56] K. Yamamoto, T. Abe, S.-I. Takasu, Thermal diffusivity of crystalline and liquid silicon and an anomaly at melting, Jpn. J. Appl. Phys. 30 (1991) 2423–2426, https://doi.org/10.1143/JJAP.30.2423.
[57] K.E. Eseller, F.-Y. Yueh, J.P. Singh, Non-intrusive, on-line, simultaneous multi-species impurity monitoring in hydrogen using LIBS, Appl. Phys. B 102 (2011) 963–969, https://doi.org/10.1007/s00340-010-4202-8.

[58] S. Almaviva, L. Caneve, F. Colao, G. Maddaluno, R. Fantoni, Accessory laboratory measurements to support quantification of hydrogen isotopes by in-situ LIBS from a robotic arm inside a fusion vessel, Spectrochim. Acta, Part B 181 (2021) 106230, https://doi.org/10.1016/j.sab.2021.106230.
[59] A. Marin Roldan, V. Dwivedi, M. Veis, S. Atikukke, H. van der Meiden, M. Drzik, P. Veis, Quantification of hydrogen isotopes by CF-LIBS in a W-based material (WZr) at atmospheric pressure: from ns towards ps, Phys. Scr. 96 (2021) 124061, https://doi.org/10.1088/1402-4896/ac35f2.
[60] P.A. Gaviola, M. Sallese, M. Suarez Anzorena, C.E. Ararat Ibarguen, A.A. Bertolo, M. Iribarren, R. Perez, E. Morel, J. Torga, A.J. Kreiner, M.F. del Grosso, Development of a simple method based on LIBS for evaluation of neutron production targets made of hydrogen isotopes, Measurement 177 (2021) 109245, https://doi.org/10.1016/j.measurement.2021.109245.
[61] B.Y. Man, Particle velocity, electron temperature, and density profiles of pulsed laser-induced plasmas in air at different ambient pressures, Appl. Phys. B 67 (1998) 241–245, https://doi.org/10.1007/s003400050500.
[62] J.S. Cowpe, J.S. Astin, R.D. Pilkington, A.E. Hill, Temporally resolved laser induced plasma diagnostics of single crystal silicon - effects of ambient pressure, Spectrochim. Acta, Part B 63 (2008) 1066–1071, https://doi.org/10.1016/j.sab.2008.09.007.
[63] J.S. Cowpe, R.D. Pilkington, J.S. Astin, A.E. Hill, The effect of ambient pressure on laser-induced silicon plasma temperature, density and morphology, J. Phys. D, Appl. Phys. 42 (2009) 165202, https://doi.org/10.1088/0022-3727/42/16/165202.
[64] M.A. Gigosos, M.A. Gonzalez, V. Cardenoso, Computer simulated Balmer-alpha, -beta and -gamma Stark line profiles for non-equilibrium plasmas diagnostics, Spectrochim. Acta, Part B 58 (2003) 1489–1504, https://doi.org/10.1016/S0584-8547(03)00097-1.
[65] S. Buscher, Th. Wrubel, S. Ferri, H.-J. Kunze, The Stark width and shift of the hydrogen H_α line, J. Phys. B, At. Mol. Opt. Phys. 35 (2002) 2889–2897, https://doi.org/10.1088/0953-4075/35/13/304.
[66] R.C. Elton, Atomic processes, in: H.R. Griem, R.H. Lovberg (Eds.), Methods of Experimental Physics, vol. 9, Academic Press, New York, 1970, pp. 115–168.
[67] R. Wilson, The spectroscopy of non-thermal plasmas, J. Quant. Spectrosc. Radiat. Transf. 2 (1962) 477–490, https://doi.org/10.1016/0022-4073(62)90033-X.
[68] H.R. Griem, Validity of local thermal equilibrium in plasma spectroscopy, Phys. Rev. 131 (1963) 1170–1176, https://doi.org/10.1103/PhysRev.131.1170.
[69] R.W.P. McWhirter, Departures from local thermodynamic equilibrium, in: R.H. Huddlestone, S.L. Leonard (Eds.), Plasma Diagnostic Techniques, Academic Press, New York, 1965, pp. 201–264.
[70] H.W. Drawin, Validity conditions for local thermodynamic equilibrium, Z. Phys. 228 (1969) 99–119, https://doi.org/10.1007/BF01397532.
[71] J.D. Hey, Criteria for local thermal equilibrium in non-hydrogenic plasmas, J. Quant. Spectrosc. Radiat. Transf. 16 (1976) 69–75, https://doi.org/10.1016/0022-4073(76)90124-2.
[72] T. Fujimoto, R.W.P. McWhirter, Validity criteria for local thermodynamic equilibrium in plasma spectroscopy, Phys. Rev. A 42 (1990) 6588–6601, https://doi.org/10.1103/PhysRevA.42.6588.
[73] G. Cristoforetti, A. De Giacomo, M. Dell'Aglio, S. Legnaioli, E. Tognoni, V. Palleschi, N. Omenetto, Local thermodynamic equilibrium in laser-induced breakdown spectroscopy: beyond the McWhirter criterion, Spectrochim. Acta, Part B 65 (2010) 86–95, https://doi.org/10.1016/j.sab.2009.11.005.
[74] H.W. Drawin, Validity conditions for local thermodynamic equilibrium, in: R. Rompe, M. Steenbeck (Eds.), Progress in Plasmas and Gas Electronics, vol. 1, Akademie-Verlag, Berlin, 1975, pp. 594–660.
[75] J. Hermann, C. Gerhard, E. Axente, C. Dutouquet, Comparative investigation of laser ablation plumes in air and argon by analysis of spectral line shapes: insights on calibration-free laser-induced breakdown spectroscopy, Spectrochim. Acta, Part B 100 (2014) 189–196, https://doi.org/10.1016/j.sab.2014.08.014.
[76] M.F. Modest, Radiative Heat Transfer, Elsevier, 2013.
[77] J. Vleck, J. Ferdinand, Collisional-radiative recombination in argon plasmas, Beitr. Plasmaphys. 24 (1984) 19–26, https://doi.org/10.1002/ctpp.19840240103.
[78] J.R. Stallcop, K.W. Billman, Analytical formulae for the inverse Bremsstrahlung absorption coefficient, Plasma Phys. 16 (1974) 1187–1189, https://doi.org/10.1088/0032-1028/16/12/008.
[79] H.R. Griem, Plasma Spectroscopy, McGraw Hill, New York, 1964.
[80] H.J. Kunze, Introduction to Plasma Spectroscopy, Springer Series on Atomic, Optical and Plasma Physics, Berlin, 2009.
[81] Z. Mijatovic, S. Djurovic, L. Gavanski, T. Gajo, A. Favre, V. Morel, A. Bultel, Plasma density determination by using hydrogen Balmer H_α spectral line with improved accuracy, Spectrochim. Acta, Part B 166 (2020) 105821, https://doi.org/10.1016/j.sab.2020.105821.
[82] L. Yang, X. Tan, X. Wan, L. Chen, D. Jin, M. Qian, G. Li, Stark broadening for diagnostics of the electron density in non-equilibrium plasma utilizing isotope hydrogen alpha lines, J. Appl. Phys. 115 (2014) 163106, https://doi.org/10.1063/1.4873960.
[83] X. Zeng, X. Mao, S.S. Mao, J.H. Yoo, R. Greif, R.E. Russo, Laser-plasma interactions in fused silica cavities, J. Appl. Phys. 95 (2004) 816–822, https://doi.org/10.1063/1.1635990.
[84] M. Hanif, M. Salik, M.A. Baig, Optical spectroscopic studies of titanium plasma produced by an Nd: YAG laser, Opt. Spectrosc. 114 (2013) 7–14, https://doi.org/10.1134/S0030400X13010116.
[85] Vasily N. Lednev, S.M. Pershin, A.A. Ionin, S.I. Kudryashov, S.V. Makarov, A.E. Ligachev, A.A. Rudenko, R.A. Chmelnitsky, A.F. Bunkin, Laser ablation of polished and nanostructured titanium surfaces by nanosecond laser pulses, Spectrochim. Acta, Part B 88 (2013) 15–19, https://doi.org/10.1016/j.sab.2013.07.010.
[86] G. Gerhard, J. Hermann, L. Mercadier, L. Loewenthal, E. Axente, C.R. Luculescu, T. Sarnet, M. Sentis, W. Viol, Quantitative analyses of glass via laser-induced breakdown spectroscopy in argon, Spectrochim. Acta, Part B 101 (2014) 32–45, https://doi.org/10.1016/j.sab.2014.07.014.
[87] J. Hermann, A. Lorusso, A. Perrone, F. Strafella, C. Dutouquet, B. Torralba, Simulation of emission spectra from nonuniform reactive laser-induced plasmas, Phys. Rev. E 92 (2015) 053103, https://doi.org/10.1103/PhysRevE.92.053103.
[88] H. Yao, E. Asamoah, P. Wei, J. Cong, L. Zhang, J.K. Quaisie, A. Asamoah, K. Ayepah, W. Zhu, Investigation into the effect of increasing target temperature and the size of cavity confinements on laser-induced plasmas, Metals 10 (2020) 393, https://doi.org/10.3390/met10030393.
[89] M. Dell'Aglio, V. Cardette, S.C. Jantzi, A. De Giacomo, Comparison between laser-induced plasmas in gas and in liquid, J. Appl. Phys. 129 (2021) 233303, https://doi.org/10.1063/5.0039625.
[90] A.A.I. Khalil, M. Richardson, L. Johnson, M.A. Gondal, Titanium plasma spectroscopy studies under double pulse laser excitation, Laser Phys. 19 (2009) 1981–1992, https://doi.org/10.1134/S1054660X09190116.
[91] S. Zhang, X. Wang, M. He, Y. Jiang, B. Zhang, W. Hang, B. Huang, Laser-induced plasma temperature, Spectrochim. Acta, Part B 97 (2014) 13–33, https://doi.org/10.1016/j.sab.2014.04.009.
[92] S. Bashir, N. Farid, K. Mahmood, M.S. Rafique, Influence of ambient gas and its pressure on the laser-induced breakdown spectroscopy and the surface morphology of laser-ablated Cd, Appl. Phys. A 104–107 (2012) 203–212, https://doi.org/10.1007/s00339-011-6730-4.
[93] J.A. Aguilera, C. Aragon, J. Bengoechea, Spatial characterization of laser-induced plasmas by deconvolution of spatially resolved spectra, Appl. Opt. 42 (2003) 5938–5946, https://doi.org/10.1364/AO.42.005938.
[94] A. Gomes, A. Aubreton, J.J. Gonzalez, S. Vacquie, Experimental and theoretical study of the expansion of a metallic vapour plasma produced by laser, J. Phys. D, Appl. Phys. 37 (2004) 689–696, https://doi.org/10.1088/0022-3727/37/5/007.
[95] J.A. Aguilera, C. Aragon, A comparison of the temperatures and electron densities of laser-produced plasmas obtained in air, argon, and helium at atmospheric pressure, Appl. Phys. A 69 (Suppl) (1999) S475–S478, https://doi.org/10.1007/s003390051443.
[96] J.A. Aguilera, J. Bengoechea, C. Aragon, Curves of growth of spectral lines emitted by a laser-induced plasma: influence of the temporal evolution and spatial inhomogeneity of the plasma, Spectrochim. Acta, Part B 58 (2003) 221–237, https://doi.org/10.1016/S0584-8547(02)00258-6.
[97] P. Roura, F. Tair, J. Farjas, P. Rocca i Cabarrocas, Measurement of the specific heat and determination of the thermodynamic functions of relaxed amorphous silicon, J. Appl. Phys. 113 (2013) 173515, https://doi.org/10.1063/1.4803888.
[98] N. Attaf, M.S. Aida, L. Hadjeris, Thermal conductivity of hydrogenated amorphous silicon, Solid State Commun. 120 (2001) 525–530, https://doi.org/10.1016/S0038-1098(01)00428-8.